

# Linear stability of a gas boundary layer flowing past a thin liquid film over a flat plate

By NIKOLAOS A. PELEKASIS  
AND JOHN A. TSAMOPOULOS

Laboratory of Computational Fluid Dynamics, Department of Chemical Engineering,  
University of Patras, Patras 26500, Greece  
e-mail: pel@chemeng.upatras.gr; tsamo@chemeng.upatras.gr

(Received 26 July 1999 and in revised form 22 September 2000)

The flow of a gas stream past a flat plate under the influence of rainfall is investigated. As raindrops sediment on the flat plate, they coalesce to form a water film that flows under the action of shear from the surrounding gas stream. In the limit of (a) large Reynolds number,  $Re$ , in the gas phase, (b) small rainfall rate,  $\dot{r}$ , compared to the free-stream velocity,  $U_\infty$ , and (c) small film thickness compared to the thickness of the boundary layer that surrounds it, a similarity solution is obtained that predicts growth of the liquid film like  $x^{3/4}$ ;  $x$  denotes dimensionless distance from the leading edge. The flow in the gas stream closely resembles the Blasius solution, whereas viscous dissipation dominates inside the film. Local linear stability analysis is performed, assuming nearly parallel base flow in the two streams, and operating in the triple-deck regime. Two distinct families of eigenvalues are identified, one corresponding to the well-known Tollmien–Schlichting (TS) waves that originate in the gas stream, and the other corresponding to an interfacial instability. It is shown that, for the air–water system, the TS waves are convectively unstable whereas the interfacial waves exhibit a pocket of absolute instability, at the streamwise location of the applied disturbance. Moreover, it is found that as the inverse Weber number ( $We^{-1}$ ) increases, indicating the increasing effect of surface tension compared to inertia, the pocket of absolute instability is translated towards larger distances from the leading edge and the growth rate of unstable waves decreases, until a critical value is reached,  $We^{-1} \approx We_c^{-1}$ , beyond which the family of interfacial waves becomes convectively unstable. Increasing the inverse Froude number ( $Fr^{-1}$ ), indicating the increasing effect of gravity compared to inertia, results in the pocket of absolute instability shrinking until a critical value is reached,  $Fr^{-1} \approx Fr_c^{-1}$ , beyond which the family of interfacial waves becomes convectively unstable. As  $We^{-1}$  and  $Fr^{-1}$  are further increased, interfacial waves are eventually stabilized, as expected. In this context, increasing the rainfall rate or the free-stream velocity results in extending the region of absolute instability over most of the airfoil surface. Owing to this behaviour it is conjectured that a global mode that interacts with the boundary layer may arise at the interface and, eventually, lead to three-dimensional waves (rivulets), or, under extreme conditions, even premature separation.

---

## 1. Introduction

Aircraft behaviour under conditions of heavy rain and high wind shear has been studied with increasing interest in the past ten years owing to a number of accidents

that have occurred under such weather conditions (Dunham 1987). Most of these accidents took place at low altitudes, while the aircraft was either landing or taking off. Extensive experimental investigations on commercial airfoils conducted by NASA (Campbell & Bezos 1989) indicate a pattern of decreasing lift capability and increasing drag coefficient with increasing intensity of rain. In addition, flow patterns captured via the use of ultraviolet strobe light reveal that, at small angles of attack, a liquid film is formed that covers the wing surface except for two regions. The first one lies near the leading edge, where droplet impact splashing takes place, whereas the second one is formed as a result of the disruption of the continuity of the film which breaks up into rivulets that run towards the trailing edge. As the angle of attack increases, the rivulets begin to form closer to the leading edge of the airfoil until, for angles of attack corresponding to stall conditions, the film disappears and the flow separates with significant performance loss. It is believed that the interaction between the thin liquid film and the surrounding boundary layer is responsible for the above pattern (Campbell & Bezos 1989). In a similar context, anti-icing fluids applied on the wing surface in order to prevent frost, ice or snow from adhering to it, can have an adverse aerodynamic effect if they fail to flow off the wing, as the plane accelerates on the runway, and leave a clean surface at the time of lift-off (van Hengst 1991).

The fundamental question raised by these effects concerns the mechanism of wave formation in the film and the fashion by which these waves interact with the boundary layer. It is understood that the wavy film layer produces an increase of the aerodynamic roughness of the wing surface thus thickening the boundary layer surrounding it. This is thought to be the dominant mechanism for lift loss (Carbonaro & Ozgen 1997). Clearly the displacement thickness is a quantity that must be related to the variation of the aerodynamic characteristics of the airfoil. However, Feo & Gonzalez (1985) found that performance degradation can also take place as a result of premature boundary layer separation caused by the interaction between the thin film and the surrounding gas stream. They used the wind tunnel facility at NASA-Langley in order to measure the evolution of film thickness on a NACA 64-210 airfoil under conditions of simulated rainfall, and were able to verify the formation of a continuous liquid film on the upper and lower airfoil surfaces for a wide range of parameters. The film thickness on the upper airfoil surface invariably exhibited a maximum in the vicinity of the position of maximum airfoil thickness followed by a reduction in magnitude until eventually its continuity was disrupted halfway along the airfoil, probably due to the formation of rivulets that evolve in the spanwise direction of the airfoil. The maximum thickness of the film was observed to become as much as twice as large as the local boundary layer thickness. Evaluation of these findings led to the plausible conjecture that the water film in the upper surface may be responsible for increased skin friction and premature boundary layer separation. Indeed, steady-state simulations of the growth of a liquid film on a model airfoil surface, for zero angle of attack, carried out by Smyrniotis, Pelekasis & Tsamopoulos (2000) indicate that such a premature boundary layer separation can occur in the presence of a liquid film but the maximum in the film thickness that characterizes its wavy shape cannot be predicted, in the relevant parameter range. Consequently, such a pattern may be part of the dynamic interaction between the film and the air stream. The early stages of this interaction, when the variation of the film thickness remains small, can be captured by linear analysis, which is the approach adopted in the present study.

Yih (1967) was the first to present an analysis for two-dimensional, long-wavelength disturbances of two superposed fluids in plane Poiseuille flow. Yih derived a general expression for the complex wave speed and showed that viscosity stratification can

give rise to an interfacial mode, which exists for arbitrarily small Reynolds numbers. He did not, however, proceed to examine the dependence of the growth rate on the parameters of the problem, such as the density ratio, or the thickness ratio of the two layers. Yiantsios & Higgins (1988) carried out a numerical study of the linear stability of plane Poiseuille flow of two superposed fluids and confirmed previous findings by various investigators, Yih (1967) and Hooper (1985) among others, according to which a thin layer of more viscous fluid adjacent to a solid boundary is linearly unstable to an interfacial mode. They did not follow this mode to very large values of the Reynolds number nor did they carry out an extensive comparison between the growth rates of this mode and those of the Tollmien–Schlichting mode, corresponding to the shear mode in their study, owing to numerical difficulties. The Tollmien–Schlichting (TS) waves originate in the bulk of the air flow and eventually lead to turbulence. Hooper & Boyd (1987) examined the flow of two superposed fluids in linear shearing motion bounded by a wall. For large values of the Reynolds number, waves longer than the thickness of the lower fluid arise, that can be longer or shorter than the thickness of the viscous sublayer in the upper fluid, depending on whether the lower fluid is more or less viscous than the upper one, respectively. Such waves arise in the context of our analysis as well. Of course, when the combination air–water is examined only the former type of wave is recovered. The third type of instability discovered by Hooper & Boyd, related to the ratio of kinematic viscosity of the two fluids, cannot be captured here because it requires a much larger value of the inner fluid thickness.

All of the above studies presented a limited comparison of the different types of waves that can arise in two-phase flow without, however, focusing on the details of boundary layer flow over a growing thin film. More recently, and in order to investigate the effect of de-/anti-icing fluids on airfoil performance, several studies have appeared that treat the basic flow as parallel and solve the Orr–Sommerfeld equations for the stability of a gas boundary layer flowing over a Newtonian (Carbonaro & Ozgen 1997), or a power law fluid (Boelens & Hoeijmakers 1997; Ozgen, Degrez & Sarma 1998). The latter two studies use a spectral method and the backward integration method (Drazin & Reid 1981), respectively, for the calculation of the frequency  $\omega$  given the wavenumber,  $\alpha$ , and the parameters of the problem (temporal stability analysis). Owing to the high Reynolds number of the flow and the complicated nature of the eigenvalue problem, numerical evaluation of the eigenvalues is quite tedious as it requires iterations (Boelens & Hoeijmakers 1997). Consequently, both studies perform temporal stability analysis relying on Gaster's (1962) transformation, which holds true mainly near the region where the imaginary parts of the eigenvalues cross zero, for the evolution of  $\alpha$  as a function of  $\omega$  (spatial stability analysis). They find that TS waves are dominant over the interfacial waves and they suggest that research should focus on creating waves that transport as much fluid as possible in order to clean the wing during take-off.

In an effort to circumvent the numerical problems associated with solving the Orr–Sommerfeld equations at large Reynolds numbers, Timoshin (1997) performed a linear stability analysis of a boundary layer developing over a thin film using triple-deck theory, and assuming parallel basic flow. In the context of temporal stability analysis he calculated the eigenfrequencies, given the wavenumber and the parameters describing the combined motion of the two fluids. In doing so, he was able to recover the interfacial modes predicted by Hooper & Boyd (1987), both when the film viscosity is greater than that of the ambient fluid—long waves stemming from a point located in the upper branch of the neutral stability curve—and when the film

viscosity is smaller—shorter scale waves stemming from a point located in the lower branch of the neutral stability curve. The concept of lower and upper neutral branch is borrowed here from the neutral stability curve discovered for TS waves (Jordinson 1970). In the former case, taking relatively large values of the wavenumber and the density ratio of the two fluids to be of  $O(1)$ , he found that the interfacial modes grow faster than the TS disturbances. A related triple-deck approach has been adopted by Tsao, Rothmayer & Ruban (1997) with application to airplane de-icing technology. They assume extremely large viscosity and density of the de-icing fluid, essentially decoupling the dynamics of the two layers and focusing on interfacial waves. In the present study we are interested in comparing the behaviour of the two modes. Therefore, we allow the density and viscosity ratios of the fluids in the two layers to remain  $O(1)$  in the analysis, in general, even though they have quite small values for the air/water system studied here. As will be seen in §5.1.2 the asymptotic solution in the limit of negligible viscosity in the gas stream significantly underpredicts the neutral stability point in the case of air/water interaction with viscosity ratio 0.018, roughly.

The primary concern of the research effort initiated by the present study is the investigation of the spatio-temporal behaviour of TS and interfacial instabilities in the context of stratified boundary layer flow while adhering to the parallel base flow assumption. The conjecture that connects this study with the experimental observations mentioned at the beginning of this section is that the onset of interfacial instability causes such intense interaction with the boundary layer that, under certain conditions, it can lead to premature separation. The nature and growth rate of interfacial and TS waves is identified and compared, whereas three-dimensional effects and the formation of rivulets are left for a future study. The proper context for studying boundary layer stability in the presence of an obstacle, in the present case the growing liquid film, when the Reynolds number is very large, is provided by the triple-deck theory by Stewartson & Williams (1969), Neiland (1969), Messiter (1970) most notably among others (for a good reference article summarizing previously obtained results regarding triple-deck theory see also Smith *et al.* 1981). In these articles the authors establish the method and give the proper characteristic length scales of the obstacle for separation to occur. As is well known for boundary layer flow past a flat plate at high Reynolds number, in the absence of the film the most amplified TS waves appear near their lower neutral branch, figure 1 in Smith (1979), and their wavelength and time scales are  $LRe^{-3/8}$ ,  $LRe^{-1/4}/U_\infty$ , respectively;  $L$  is the characteristic length scale along the plate. In this range of wavelengths the flow consists of a viscous layer, the lower deck, that is attached to the wall and whose thickness is of order  $LRe^{-5/8}$ . This layer is embedded in an order  $LRe^{-1/2}$  inviscid yet rotational layer, the main deck, and that in turn is embedded in the order  $LRe^{-3/8}$  upper deck where potential flow conditions exist, figure 1. As was pointed out by Smith *et al.* (1981), the smallest size,  $H_f$ , of an obstacle of length  $\lambda \sim LRe^{-3/8} \ll L$ , that can cause large-scale separation of the flow is that with height that belongs to the triple-deck regime,  $H_f \sim LRe^{-5/8}$ . We would like to investigate this possibility in the context of the present problem. For this reason, given the length scale  $L$ , the rainfall rate,  $\dot{r}$ , the free-stream velocity,  $U_\infty$ , and the physical properties of the gas stream—density  $\rho$  and viscosity  $\mu$ ,  $Re = LU_\infty\rho/\mu$ —and the water film—density  $\rho_w$  and viscosity  $\mu_w$ —we choose to study a case with characteristic film thickness  $H_f$  and wavelength  $\lambda$  corresponding to the triple-deck regime. A characteristic value for  $H_f$  is given in §2. With this formulation the TS waves, modified by the presence of the film, as well as the interfacial waves, can be captured. The evolution of the basic

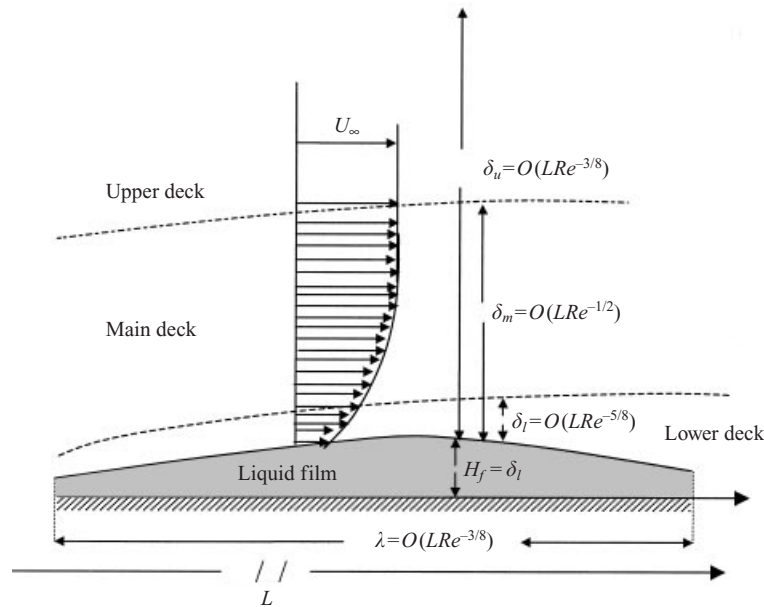


FIGURE 1. Schematic representation of the triple-deck structure of the flow.

flow with the distance from the leading edge,  $x$ , is neglected in the present order of approximation, while the analysis is limited to linear disturbances, leaving global spatial development and nonlinear growth to a future treatment. It should also be noted that, if needed, turbulent boundary layers may be examined by considering the appropriate mean velocity distribution, Benjamin (1958).

The triple-deck approach undertaken in the present study is similar to the one presented by Timoshin (1997), with the difference that here the focus is on distinguishing between spatially developing modes and absolutely unstable modes that grow with time. It should also be noted that the base flow used here differs from that adopted by Timoshin in that we allow for an increasing film thickness, whereas he employs the constant volumetric flow rate solution provided by Nelson, Alving & Joseph (1995) leading to a film thickness that decays with increasing distance from the leading edge. In view of the non-parallel nature of the basic flow, a local stability analysis is undertaken that examines the evolution of unstable waves around a selected position  $x_0$  of the basic flow where the disturbance is applied. Such waves are characterized by a length scale  $\lambda \ll L$ , which amounts to assuming nearly parallel basic flow conditions. In order to simulate disturbances normally applied in experiments the response of the system to an impulse in space and time is investigated. This approach was originally proposed by Briggs (1964) in the context of plasma physics, and has received increased attention in the field of fluid mechanics; see e.g. the review article by Huerre & Monkewitz (1990). It is then possible to characterize the response of the system to an impulse, at each streamwise location within the parallel flow approximation, as locally absolutely unstable when localized disturbances spread upstream and downstream and contaminate the entire parallel flow, whereas it is locally convectively unstable when localized disturbances are swept away from the source. The convective or absolute nature of unstable waves is determined via the ‘pinching’ method, Briggs (1964), which looks for algebraic branch points of the complex dispersion relation  $\alpha(\omega)$  in the complex  $\omega$ -plane where the group velocity,  $d\omega/d\alpha$ , equals

zero. Special emphasis is placed on the topography of the spatial branches emanating from the branch point, at least two of which must lie in distinct halves of the complex  $\alpha$ -plane when  $\omega_i$  is sufficiently large and positive, Lingwood (1997). It will be seen in the last section of the present study that, when impulsive disturbances are applied, interfacial waves can be as important, if not more important, than TS waves in determining the stability of the system owing to the absolutely unstable nature of the former type of waves.

Since we are primarily interested in the effect of rainfall on boundary layer stability, we will focus on the case of steady laminar flow of an air stream at high Reynolds number over a water film that grows on a flat plate. This is a first step towards a qualitative understanding of the mechanism of lift loss, so we neglect the effect of varying angle of attack or finite curvature of the geometry, leaving these issues to another study. In §2 the governing equations describing steady development of a boundary layer over a growing film are presented in the limit as  $Re \rightarrow \infty$  and  $H_f/L \ll 1$ . In §2.1 the simplified equations and the corresponding similarity solution are given when  $H_f/(LRe^{-1/2}) \ll 1$ . Next, in §3 the equations describing the dynamic condition of the system are given, first taking into consideration the nonlinear interaction between the fluid film and the viscous sublayer, §3.1, whereas in §3.2 the linearized triple-deck equations are presented via a stream function formulation. In §4 the numerical method used for the solution of the linear stability problem is described, §4.1, as well as the ‘pinching’ method used for identifying the algebraic branch points in the dispersion relation, §4.2. The results of linear stability analysis are presented in §5. The absolute/convective character of the unstable TS and interfacial waves is discussed and compared in §5.1.1 and §5.1.2, and comparison is made with previous studies. Finally, in §5.2 a parametric study is presented that accounts for the effects of surface tension and gravity on the stability of the air–water system and specific conclusions are drawn for the problem of rainfall.

## 2. Problem formulation at steady state

We wish to examine two-dimensional laminar flow of air past a flat plate, under conditions of rainfall. More specifically, we are interested in obtaining a quantitative description of water-film formation and growth and, subsequently, of wave development at the gas–liquid interface. Two-dimensional analysis will suffice for the investigation of the system stability, especially during the initial stages of wave formation. Far from the plate, the air velocity assumes its free-stream value,  $U_\infty$ , parallel to the plate (zero angle of attack) and at right angles to gravity. In order to simulate rainfall conditions the air stream is assumed to be carrying raindrops which, as they sediment on the plate, coalesce and form a thin water film that covers the plate entirely and is forced to flow under the action of shear from the air stream, figure 2. The raindrop size is taken to be very small so that particle inertia can be neglected. Consequently it is permissible to treat raindrops as spherical undeformable particles, Happel & Brenner (1986, p. 129). In this context, and following Pelekasis & Acrivos (1995), we obtain the following equation for the mass balance of the rain particles at the interface:

$$\phi_s \mathbf{n} \cdot \mathbf{U}' + f(\phi_s) \phi_s u_t \mathbf{e}_g \cdot \mathbf{n} = \mathbf{u}' \cdot \mathbf{n}, \quad (2.1)$$

where  $f(\phi_s) = 1 - \phi_s$  is a hindrance function accounting for the influence of particle interactions on the terminal velocity of individual particles when the raindrop concentration,  $\phi_s$ , inside the bulk of the air stream is small,  $u_t$  is the Stokes terminal

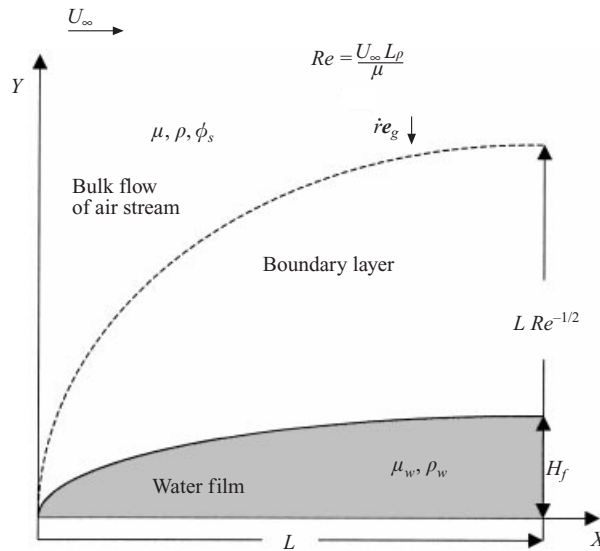


FIGURE 2. Schematic representation of the steady boundary layer flow.

velocity of raindrops,  $\mathbf{e}_g$  is the unit vector in the direction of gravity,  $\mathbf{n}$  is the normal vector at the air–water interface, and  $\mathbf{U}'$ ,  $\mathbf{u}'$ , denote the dimensional velocities in the bulk of the gas stream and the film, respectively. In the following, variables in capital letters correspond to quantities defined in the gas phase, variables in lower-case letters refer to the water film whereas primed variables denote variables with dimensions. Equation (2.1) reflects the fact that raindrops possess a slip velocity relative to the bulk motion of the gas stream which, in the limit of negligible inertia of the raindrops, is given by the Stokes terminal velocity  $u_t$  corrected by the hindrance function  $f(\phi_s)$ . In the same limit of negligible raindrop inertia the total velocity of raindrops in the air stream, with respect to an inertial frame of reference, is the superposition of the bulk velocity of the gas stream and their slip velocity. It is this slip velocity that determines the formation and growth of the interface. Upon application of the continuity of bulk normal velocities on either side of the interface we obtain

$$\dot{r} \mathbf{e}_g \cdot \mathbf{n} = u'_n, \tag{2.2}$$

where  $\dot{r} = u_t \phi_s$  is the rainfall rate in  $\text{ms}^{-1}$ . More details on the model adopted for rainfall, along with a more general formulation of the steady flow of the air stream–water film system past curvilinear surfaces are given in Smyrniotis *et al.* (2000).

To describe the steady state of the boundary layer flow of an air stream that develops above a growing film of water we introduce the following natural scalings, bearing in mind that the air stream flows at high speed,  $Re \gg 1$ , while driving to motion the more viscous film of water,  $H_f \ll L$ ,  $u_f \ll U_\infty$ ;  $H_f$ ,  $u_f$  are the reference liquid film thickness and velocity parallel to the plate, respectively, to be estimated later. More specifically, the following dimensionless quantities are used as scales:  $L$  and  $LRe^{-1/2}$  as characteristic length scales of the boundary layer type in the gas phase and in the direction parallel,  $x$ , and perpendicular,  $\bar{Y}$ , to the plate, respectively;  $U_\infty$  and  $U_\infty Re^{-1/2}$  as characteristic velocities along the  $x$ - and  $\bar{Y}$ -directions in the gas phase, respectively;  $L$  and  $H_f$  as characteristic length scales in the liquid film in the direction parallel,  $x$ , and perpendicular,  $y$ , to the plate, respectively;  $u_f$  and  $u_f(H_f/L)$  as characteristic velocities along the  $x$ - and  $y$ -directions in the film, respectively.

Finally, the inertial scale,  $\rho U_\infty^2$ , is used for the pressure in both the gas,  $P$ , and the liquid,  $p$ , phases, while  $H_f$  is used as a measure of the film thickness  $H$ . It should also be noted that the gravitational force acting in the gas phase is incorporated in the pressure term in both phases,

$$P + \frac{g\bar{Y}LRe^{-1/2}}{U_\infty^2} \rightarrow P, \quad p + \frac{gyH_f}{U_\infty^2} \rightarrow p. \quad (2.3)$$

This ensures that the total pressure in the gas phase,  $P$ , vanishes in the limit  $\bar{Y} \rightarrow \infty$ , and introduces the effect of varying density across the interface in the momentum equation of the film. In the following subscript  $s$  refers to dimensionless quantities at steady state. In this context and ignoring terms which are  $O(Re^{-1/2})$ ,  $O(H_f/L)$ , or smaller, the governing equations inside the gas phase become:

continuity

$$\frac{\partial U_s}{\partial x} + \frac{\partial V_s}{\partial \bar{Y}} = 0; \quad (2.4)$$

$x$ - and  $\bar{Y}$ -momentum

$$U_s \frac{\partial U_s}{\partial x} + V_s \frac{\partial U_s}{\partial \bar{Y}} = -\frac{\partial P_s}{\partial x} + \frac{\partial^2 U_s}{\partial \bar{Y}^2}, \quad \frac{\partial P_s}{\partial \bar{Y}} = 0; \quad (2.5a, b)$$

far-field condition

$$\bar{Y} \rightarrow \infty, \quad U_s \rightarrow 1, \quad P_s \rightarrow 0, \quad (2.6)$$

at the interface,  $\bar{Y} = (H_f/LRe^{-1/2})H_s(x)$ ,  $y = H_s(x)$ ;

continuity of the tangential and normal velocities

$$U_s = \frac{u_f}{U_\infty} u_s, \quad V_s = \frac{u_f}{U_\infty} \frac{H_f}{LRe^{-1/2}} v_s; \quad (2.7a, b)$$

continuity of the tangential and normal stresses

$$\frac{1}{Re^{-1/2}} \frac{\partial U_s}{\partial \bar{Y}} = \frac{u_f}{U_\infty} \frac{\mu_w}{\mu} \frac{L}{H_f} \frac{\partial u_s}{\partial y}, \quad P_s = p_s; \quad (2.8a, b)$$

interfacial mass balance

$$u_s \frac{dH_s}{dx} - v_s = \frac{\dot{r}L}{u_f H_f}. \quad (2.9)$$

In the liquid film they are:

continuity and  $y$ -momentum

$$\frac{\partial u_s}{\partial x} + \frac{\partial v_s}{\partial y} = 0, \quad \frac{\partial p_s}{\partial y} = -\frac{gH_f}{U_\infty^2} \left( \frac{\rho_w}{\rho} - 1 \right); \quad (2.10a, b)$$

$x$ -momentum

$$\left( \frac{u_f}{U_\infty} \right)^2 \frac{\rho_w}{\rho} \left( u_s \frac{\partial u_s}{\partial x} + v_s \frac{\partial u_s}{\partial y} \right) = -\frac{\partial p_s}{\partial x} + \frac{\mu_w}{\mu} \frac{u_f}{U_\infty} \frac{1}{Re} \left( \frac{L}{H_f} \right)^2 \frac{\partial^2 u_s}{\partial y^2}; \quad (2.11)$$

no-slip, no penetration at the plate

$$y = 0, \quad u_s = v_s = 0. \quad (2.12)$$

The requirement that both sides of (2.8a) and (2.9) balance each other provides us

with an estimate for the thickness,  $H_f$ , and velocity,  $u_f$ , in the film,

$$\frac{H_f}{L} = Re^{-1/4} \left( \frac{\mu_w}{\mu} \right)^{1/2} \left( \frac{\dot{r}}{U_\infty} \right)^{1/2}, \quad (2.13)$$

$$\frac{u_f}{U_\infty} = Re^{1/4} \left( \frac{\mu}{\mu_w} \right)^{1/2} \left( \frac{\dot{r}}{U_\infty} \right)^{1/2}. \quad (2.14)$$

The above scalings essentially equate the growth rate of the film thickness in the direction of the gas stream with the rainfall rate, and set the characteristic longitudinal film velocity so that the film sustains the shear rate that is exerted upon it by the gas stream. For the steady-state analysis the effect of surface tension on the normal force balance is neglected owing to the small value of the inverse Weber number,  $We^{-1} = (\sigma/\rho U_\infty^2)/(H_f/L^2)$ . For a wing section with length  $L \approx 30$  cm, a gas stream with free-stream velocity  $10 \text{ m s}^{-1}$ , and relatively low rainfall rate,  $\dot{r} \approx 0.001 \text{ cm s}^{-1}$ , (2.13) and (2.14) give an estimate for the film thickness and velocity of  $H_f \approx 0.1 \text{ mm}$  and  $u_f \approx 0.003 \text{ m s}^{-1}$ , respectively. For the same set of parameters  $H_f/(LRe^{-1/2}) \approx 0.15$ . As the rainfall rate increases this ratio increases as well.

2.1. Solution in the limit  $H_f/(LRe^{-1/2}) \rightarrow 0$

As was seen in the previous section, the thickness of the film is normally much smaller than that of the surrounding boundary layer. Consequently, and as a first step in the analysis, we take  $H_f/(LRe^{-1/2})$  to be very small in order to obtain the zeroth-order solution in this limit. As a result the governing equations in the gas phase admit the usual Blasius similarity solution. With  $\eta = \bar{Y}/x^{1/2}$ , we let  $U_0 = dF/d\eta$  and obtain

$$2 \frac{d^3 F}{d\eta^3} + F \frac{d^2 F}{d\eta^2} = 0, \quad F \rightarrow 1, \quad \eta \rightarrow \infty; \quad F = \frac{dF}{d\eta} = 0, \quad \eta = 0; \quad (2.15)$$

whereas the equations in the film become

$$\frac{\partial u_0}{\partial x} + \frac{\partial v_0}{\partial y} = 0, \quad \frac{\partial^2 u_0}{\partial y^2} = 0, \quad \frac{\partial p_0}{\partial y} = -\frac{gH_f}{u_f^2} \left( \frac{\rho_w}{\rho} - 1 \right) \quad (2.16a, b, c)$$

with boundary conditions

$$y = 0, \quad u_0 = v_0 = 0, \quad (2.17)$$

and at the interface,  $\bar{Y} = 0, y = H_0(x)$ ,

$$\frac{\partial u_0}{\partial y} = \frac{0.332}{\sqrt{x}}, \quad u_0 \frac{dH_0}{dx} - v_0 = 1, \quad (2.18a, b)$$

$$P_0 = 0, \quad p_0 = (H_0(x) - y) \frac{gH_f}{u_f^2} \left( \frac{\rho_w}{\rho} - 1 \right). \quad (2.19)$$

The above set of equations for the water film also admits a similarity solution of the form

$$H_0(x) = x^{3/4} \sqrt{\frac{2}{0.332}}, \quad u_0 = x^{1/4} z \sqrt{0.664}, \quad v_0 = \frac{z^2}{2}, \quad z = \frac{y}{H_0(x)}. \quad (2.20)$$

Clearly then, in this limit, simple shear flow conditions prevail in the film. The steady solution obtained in this fashion can be viewed as the leading term in an expansion

in terms of powers of  $H_f/LRe^{-1/2} \equiv \varepsilon$ :

$$\left. \begin{aligned} U_s &= U_0 + \varepsilon U_1 + O(\varepsilon^2), & V_s &= V_0 + O(\varepsilon), & P_s &= 0, & H_s &= H_0 + O(\varepsilon), \\ u_s &= u_0 + O(\varepsilon), & v_s &= v_0 + O(\varepsilon), \\ p_s &= \left(\varepsilon \frac{\mu}{\mu_w}\right)^2 p_0 + O(\varepsilon^3) = \left(\varepsilon \frac{\mu}{\mu_w}\right)^2 \frac{H_0(x) - y}{Fr} \left(\frac{\rho_w}{\rho} - 1\right) + O(\varepsilon^3), \end{aligned} \right\} \quad (2.21)$$

where

$$p_0 = \frac{p'}{\rho u_f^2}, \quad Fr = \frac{u_f^2}{g H_f}. \quad (2.22)$$

Details on the derivation of the asymptotic expansion, along with a numerical solution valid even when  $H_f/(LRe^{-1/2}) = O(1)$ , are given in Smyrniotis *et al.* (2000). At this point it is sufficient to point out that  $U_1$  is obtained as part of the solution to the linearized boundary layer equations with non-vanishing slip velocity at the interface. It arises in the  $O(\varepsilon)$  correction to the tangential velocity continuity equation, (2.7a), and it is needed for the dynamic analysis that follows in the next section. In particular, its value at the interface is used for the description of the base state of the system in the viscous sub-layer at  $t = 0$  and is

$$U_1(x_0, \bar{Y} = 0) = \frac{\mu}{\mu_w} u_0(x_0, z = 1). \quad (2.23)$$

It should also be noted that in the rest of the paper the dynamic state of the air–water system will be signified by the following hatted variables, which contain both the base and disturbance flow fields:

$$\hat{U} = \frac{U'}{U_\infty}, \quad \hat{V} = \frac{V'}{U_\infty}, \quad \hat{P} = \frac{P'}{\rho U_\infty^2}, \quad \hat{u} = \frac{u'}{U_\infty}, \quad \hat{v} = \frac{v'}{U_\infty}, \quad \hat{p} = \frac{p'}{\rho U_\infty^2}, \quad \hat{H} = \frac{H'}{H_f}. \quad (2.24)$$

Some of these definitions are different from those used for the steady-state solution, but in this way the same reference state is introduced in the different regions of the flow in order to facilitate comparison of magnitudes of all variables.

### 3. Stability analysis

#### 3.1. Triple-deck formulation

As was pointed out in the introduction, the fastest growing disturbances in boundary layer flow are those corresponding to the triple-deck scale. Therefore, for a plate with characteristic length  $L$  the appropriate local variable for the description of the stability of the flow, at a given station  $x' = x'_0$  of the basic flow, is the short scale coordinate  $X = (x' - x'_0)/\lambda$ , where  $\lambda = LRe^{-3/8}$ . Then, following Smith *et al.* (1981), the shortest film thickness,  $H_f$ , for which the interaction between the film and the gas stream can cause large-scale flow separation is the one that is comparable to the thickness of the viscous sublayer in the gas phase,  $\lambda^{1/3} L^{2/3} Re^{-1/2}$ , and because  $\lambda = LRe^{-3/8}$ , it follows that  $H_f = LRe^{-5/8}$ . Consequently, setting  $H_f = LRe^{-5/8}$  in conjunction with (2.13) provides a characteristic length scale of the problem,  $L$ , which is not necessarily equal to the length of the plate, with  $\varepsilon = H_f/(LRe^{-1/2}) = Re^{-1/8}$  as the small variable used for the asymptotic description of the flow in triple-deck theory. It is important to note that the triple-deck formulation can also capture the evolution of waves that are longer or shorter than  $LRe^{-3/8}$ , provided that  $H_f \ll \lambda$ , by appropriate rescaling

of the triple-deck equations. Since we are interested in disturbances that arise in the vicinity of the film–air interface their appropriate time scale is  $\lambda/u_f$ , where  $u_f$  is the characteristic velocity of the base and disturbance fields in the liquid film, and subsequently the fast time variable is defined as

$$T = \frac{u_f t'}{\lambda} = \frac{\mu}{\mu_w} \frac{U_\infty H_f t'}{L Re^{-1/2} L Re^{-3/8}} = \frac{\mu}{\mu_w} \left( \frac{t' U_\infty}{L} \right) \varepsilon^{-2} = \frac{\mu}{\mu_w} \frac{t}{\varepsilon^2}. \tag{3.1}$$

In order to introduce the disturbance a certain location  $x_0 = x'_0/L$  on the plate is chosen. Since the local coordinate  $X$  varies on a much shorter length scale, longitudinal variations of the basic flow are negligible when compared to those of the secondary flow,  $\partial/\partial X = (\partial/\partial x)(\lambda/L)$ , and consequently the former is treated as though it were parallel (parallel base flow assumption). The structure of the disturbance flow field in the gas phase is then characterized by three distinct regions, as was mentioned in the introduction, figure 1. The dimensionless velocity and pressure in each deck are signified by  $(U, V, P)$ ,  $(\bar{U}, \bar{V}, \bar{P})$ , and  $(\tilde{U}, \tilde{V}, \tilde{P})$ , respectively.

The lower deck, the one attached to the interface, is the viscous sublayer and it is the region where strong interaction between the two phases takes place. Its thickness is of order  $L Re^{-5/8}$  and the fluid velocity and pressure scale as

$$\hat{U} = \frac{\mu}{\mu_w} \varepsilon U(X, Y, T) + O(\varepsilon^2), \quad \hat{V} = \frac{\mu}{\mu_w} \varepsilon^3 V(X, Y, T) + O(\varepsilon^4), \quad \hat{P} = \left( \frac{\mu}{\mu_w} \varepsilon \right)^2 P(X, T), \tag{3.2}$$

with  $Y = y'/(L Re^{-5/8})$ . The particular scalings arise as a result of the balance between convection, viscous dissipation and pressure of the disturbance flow field in the vicinity of the interface. The appearance of the group  $\varepsilon\mu/\mu_w$  indicates that the proper scalings for velocity and pressure in the lower deck are  $u_f$  and  $\rho u_f^2$ , respectively. It should also be noted that the base velocity of the boundary layer, as seen on the scale of the lower deck, is  $O(\varepsilon)$ , i.e. it is of the same order of magnitude as the disturbance velocity  $U$ . This behaviour is reflected in the form of the lower-deck description of the flow, (3.2), and the initial condition for the disturbance velocity in the lower deck, (3.18) below. Substituting in the momentum and continuity equations and neglecting higher-order terms we get

$$\frac{\mu}{\mu_w} \left( \frac{\partial U}{\partial T} + U \frac{\partial U}{\partial X} + V \frac{\partial U}{\partial Y} \right) = - \frac{\partial P}{\partial X} \frac{\mu}{\mu_w} + \frac{\partial^2 U}{\partial Y^2}, \tag{3.3}$$

$$\frac{\partial U}{\partial X} + \frac{\partial V}{\partial Y} = 0, \quad \frac{\partial P}{\partial Y} = 0. \tag{3.4}$$

The main deck is located immediately above the viscous sublayer. The flow in it is inviscid, but rotational, its thickness is of the order of the thickness of the boundary layer at base state, i.e.  $L Re^{-1/2}$ ,  $\bar{Y} = y'/(L Re^{-1/2})$ , while velocity and pressure inside it scale as

$$\left. \begin{aligned} \hat{U} &= U_0(x, \bar{Y}) + \varepsilon \left( \frac{\mu}{\mu_w} \bar{U}(X, T, \bar{Y}) + U_1(x, \bar{Y}) \right) + O(\varepsilon^2), \\ \hat{V} &= Re^{-1/2} V_0(x, \bar{Y}) + \varepsilon^2 \frac{\mu}{\mu_w} \bar{V}(X, \bar{Y}, T) + O(\varepsilon^3), \quad \hat{P} = \left( \varepsilon \frac{\mu}{\mu_w} \right)^2 \bar{P} + O(\varepsilon^3), \end{aligned} \right\} \tag{3.5}$$

Clearly the longitudinal component of the disturbance velocity field is of higher order than the base state, whereas the opposite is true with the transverse part. In this

fashion the main deck equations take the form

$$U_0 \frac{\partial \bar{U}}{\partial X} + \bar{V} \frac{\partial U_0}{\partial \bar{Y}} = 0, \quad \frac{\partial \bar{U}}{\partial X} + \frac{\partial \bar{V}}{\partial \bar{Y}} = 0, \quad \frac{\partial \bar{P}}{\partial \bar{Y}} = 0. \quad (3.6)$$

Owing to the particular form of the above set of equations their solution is of the form

$$\bar{U} = A(X) \frac{\partial U_0}{\partial \bar{Y}}, \quad \bar{V} = -\frac{\partial A}{\partial X} U_0. \quad (3.7)$$

The longitudinal velocity has to match as the lower deck merges with the main deck. This gives

$$U(Y \rightarrow \infty) = A(X) \frac{\partial U_0}{\partial \bar{Y}}(x_0, \bar{Y} = 0) + \frac{\mu_w}{\mu} \left[ \frac{\partial U_0}{\partial \bar{Y}}(x_0, \bar{Y} = 0) Y + U_1(x_0, \bar{Y} = 0) \right], \quad (3.8)$$

with  $A(X)$  interpreted as a displacement thickness due to the viscous sublayer, and  $U_1$  given by (2.24). The terms appearing in the above equation are obtained by letting the main-deck description of the longitudinal velocity approach zero and then expressing the transversal coordinate in the main deck,  $\bar{Y}$ , in terms of the inner variable,  $Y$ . This balance, in conjunction with continuity, provides the scalings for velocity and pressure in this layer, equation (3.5).

In the upper deck potential flow conditions prevail, the characteristic length scale in the  $y$ -direction is  $LRe^{-3/8}$ ,  $\bar{\bar{Y}} = y'/(LRe^{-3/8})$ , and the velocity and pressure scale as

$$\hat{U} = 1 + \varepsilon^2 \bar{\bar{U}}(X, \bar{\bar{Y}}, T) + O(\varepsilon^3), \quad \hat{V} = \varepsilon^2 \bar{\bar{V}}(X, \bar{\bar{Y}}, T) + O(\varepsilon^3), \quad \hat{P} = \varepsilon^2 \bar{\bar{P}}(X, T) + O(\varepsilon^3), \quad (3.9)$$

the particular scalings being determined by the requirement that the normal velocity match as the main and upper decks merge. Substituting in the governing equations we obtain for the upper deck

$$\frac{\partial^2 \bar{\bar{P}}}{\partial X^2} + \frac{\partial^2 \bar{\bar{P}}}{\partial \bar{\bar{Y}}^2} = 0, \quad \frac{\partial \bar{\bar{V}}}{\partial X} = -\frac{\mu}{\mu_w} \frac{\partial \bar{\bar{P}}}{\partial \bar{\bar{Y}}}, \quad \bar{\bar{Y}} \rightarrow \infty, \quad \bar{\bar{P}} \rightarrow 0. \quad (3.10)$$

The pressure is then given by the solution of Laplace's equation in the form of an integral equation. Making use of the boundary condition at infinity, equation (3.10), as well as the relationship between the pressure and the transverse velocity in the limit as the upper deck merges with the main deck, the pressure at the gas-liquid interface becomes

$$\bar{\bar{P}} = \frac{1}{\pi} \int_{-\infty}^{\infty} \frac{\partial A}{\partial s} \frac{ds}{X-s}. \quad (3.11)$$

This pressure variation in  $X$  is imposed throughout the lower and main decks (to order  $\varepsilon^2$ ).

In the liquid film the scalings of the longitudinal velocity and the location of the interface remain the same as for steady flow, while the pressure is imposed by the gas phase,

$$\left. \begin{aligned} \hat{u} &= \frac{\mu}{\mu_w} \varepsilon u(X, y, T) + O(\varepsilon^2), & \hat{v} &= \frac{\mu}{\mu_w} \varepsilon^3 v(X, y, T) + O(\varepsilon^4), \\ \hat{p} &= \left( \varepsilon \frac{\mu}{\mu_w} \right)^2 p(X, T) + O(\varepsilon^3), & \hat{H} &= H(X, T). \end{aligned} \right\} \quad (3.12)$$

As will be seen at the end of this section the base-flow longitudinal velocity, the

pressure, and the film thickness are of the same order as their dynamic counterparts and are equal at  $T = 0$ . On the other hand the transversal velocity of the disturbance field, whose scale is set by continuity to  $\varepsilon^3$ , is much larger than the base transversal velocity which scales as  $(u_f/U_\infty)(H_f/L) = O(\varepsilon^6)$ . Hence  $v(T = 0)$  is set to zero. Next, substituting (3.12) in the governing equations we obtain

$$\frac{\rho}{\rho_w} \frac{\mu}{\mu_w} \left( \frac{\partial u}{\partial T} + u \frac{\partial u}{\partial X} + v \frac{\partial u}{\partial y} \right) = -\frac{\mu}{\mu_w} \frac{\partial p}{\partial X} - \frac{gH_f}{u_f^2} \left( \frac{\rho_w}{\rho} - 1 \right) \frac{\partial H}{\partial X} + \frac{\mu_w}{\mu} \frac{\partial^2 u}{\partial y^2}, \quad (3.13)$$

$$\frac{\partial u}{\partial X} + \frac{\partial v}{\partial y} = 0, \quad \frac{\partial p}{\partial y} = 0, \quad (3.14)$$

with boundary conditions at the plate,

$$y = 0, \quad u = v = 0, \quad (3.15)$$

and at the gas-liquid interface,  $y = Y = H(X, T)$ ,

$$U = u, \quad V = v, \quad \frac{\mu}{\mu_w} \frac{\partial U}{\partial Y} = \frac{\partial u}{\partial y}, \quad P - p = \frac{\sigma}{\rho u_f^2 H_f} \varepsilon^2 \frac{d^2 H}{dX^2}, \quad \frac{\partial H}{\partial T} + \left( u \frac{\partial H}{\partial X} - v \right) = 1. \quad (3.16)$$

The initial conditions of the disturbed flow in each deck, to leading order in  $\varepsilon$ , are derived from the equivalent base flow conditions, to the same order in  $\varepsilon$ , and are

$$\left. \begin{aligned} A(T = 0) = P(T = 0) = 0, \quad p(T = 0) = p_0(x_0, y), \\ H(T = 0) = H_0(x_0), \quad \bar{U}(T = 0) = \bar{\bar{U}}(T = 0) = 0, \\ U(T = 0) = \frac{\mu}{\mu_w} \left[ Y \frac{\partial U_0}{\partial \bar{Y}}(x_0, \bar{Y} = 0) + U_1(x_0, \bar{Y} = 0) \right] + U_D, \end{aligned} \right\} \quad (3.17)$$

$$u(T = 0) = u_0(x_0, y), \quad v(T = 0) = 0. \quad (3.18)$$

In the above  $U_D$  denotes a disturbance in the base velocity profile that will stimulate secondary motion. It can have the form of an impulse, as required for the spatio-temporal analysis that will follow. As shown in (3.18) and indicated by the base-flow solution presented in §2.1, the motion in the film and the lower deck is initially described as a simple shear. The above set of equations constitutes the description of the nonlinear behaviour of the system. The general framework of the analysis is provided by earlier studies, Stewartson & Williams (1969), Smith (1979), establishing the range of validity of triple-deck theory in the context of boundary layer stability. It should also be noted that the procedure adopted here for obtaining the stability equations follows closely the one presented by Timoshin (1997); however, the final equations shown here are slightly different because they are adapted for the particular choice of dimensionless variables and the different base flow used in the present study.

### 3.2. Linear stability analysis

The primary concern of the present study is to follow the behaviour of the system in response to infinitesimal disturbances. As was pointed out in the introduction, because the basic flow is spatially developing we have to be able to distinguish between the ranges of applicability of temporal and spatial theory. In the study of boundary layer instabilities, stability is often determined by periodically forcing the flow at a given frequency. This is the so-called signalling problem characterized by a disturbance of the form  $\delta(x - x_0)e^{i\omega_f t} H(t)$ ;  $\delta(x)$  and  $H(t)$  denote the Dirac delta

and the step function, respectively. Experimental results then seem to follow much more closely the predictions of spatial theory, where the frequency  $\omega$  is real and the wavenumber  $\alpha$  is complex, Gaster (1965). Following the terminology introduced by Briggs (1964) and Bers (1975) in distinguishing between absolutely and convectively unstable media in plasma physics, we study the response of the flow to an impulsive disturbance of the form  $\delta(x - x_0)\delta(t)$ . Motivated by the findings of previous studies in this context, Gaster (1965) for boundary layers, Huerre & Monkewitz (1985) for free shear flows, Lingwood (1995) for rotating-disk boundary layer flow, we will determine the asymptotic nature of instabilities in the limits  $X \rightarrow \infty$  or  $T \rightarrow \infty$ , by examining the branch-point singularities of the dispersion relation for complex frequencies,  $\omega$ , and wavenumbers,  $\alpha$ .

In order to obtain the dispersion relation a disturbance field is superposed on the base flow, as described via equations (3.17) and (3.18). The disturbed flow field is of the form

$$\left. \begin{aligned} U &= \frac{\mu}{\mu_w} \left[ Y \frac{\partial U_0}{\partial \bar{Y}}(\bar{Y} = 0) + U_1(\bar{Y} = 0) \right] + \delta U_{D1} + \cdots, & V &= \delta V_{D1} + \cdots, \\ P &= \delta P_{D1} + \cdots, & A &= \delta A_{D1} + \cdots, \end{aligned} \right\} \quad (3.19)$$

$$u = u_0 + \delta u_{D1} + \cdots, \quad v = \delta v_{D1} + \cdots, \quad H = H_0 + \delta H_{D1} + \cdots, \quad p = p_0 + \delta p_{D1} + \cdots, \quad (3.20)$$

with  $\delta$  a measure of the magnitude of the linear disturbance,  $\delta \ll 1$ , and subscript  $D$  introduced in order to distinguish linearized flow disturbances from steady-state corrections. It should be pointed out that since disturbances in the main and upper decks are intimately related to disturbances in the displacement thickness,  $A$ , and pressure,  $P$ , through equations (3.7) and (3.11), they need not be considered separately. Thus, introducing the disturbance pressure in the  $x$ -momentum of the lower deck, imposed by the upper-deck solution, and properly accounting for boundary condition (3.11), allows the description of the linear behaviour of the system by solving the linearized formulation inside the lower deck and the film only.

Next, a transformation is introduced that transfers the origin of the new coordinate system to the location of the interface at steady state,

$$\frac{y - H_0(x_0)}{H_0(x_0)} \rightarrow y, \quad \frac{Y - H_0(x_0)}{H_0(x_0)} \rightarrow Y. \quad (3.21)$$

The time-dependent location of the interface in the new coordinate system is then

$$y = Y = \frac{H_0 + \delta H_{D1} + \cdots - H_0}{H_0} = \delta \frac{H_{D1}}{H_0} + O(\delta^2) = \delta \hat{h}_1 + O(\delta^2), \quad (3.22)$$

The linearized set of equations that is produced after dropping higher-order terms in  $\delta$  is further modified through the introduction of stream functions,  $\Phi_1$ ,  $\Psi_1$ , in the lower deck of the gas and in the liquid phase, respectively. Next, all the variables are recast in normal mode form,

$$\Phi_1 = \Phi(Y) e^{i(\alpha X/H_0 - \omega T/H_0)}, \quad \Psi_1 = \Psi(Y) e^{i(\alpha X/H_0 - \omega T/H_0)}, \quad \hat{h}_1 = \hat{h} e^{i(\alpha X/H_0 - \omega T/H_0)}, \quad (3.23)$$

where it is understood that the eigenvectors,  $\Phi$ ,  $\Psi$ , and the variables,  $\hat{h}$ ,  $\omega$ ,  $\alpha$ , all may depend on  $x$  and  $t$  also. However, this is a higher-order effect and we need not account for it at this stage of the analysis. Finally, the equations describing the linear

stability of the system are in the gas phase

$$\frac{d^4\Phi}{dY^4} + iH_0 \frac{\mu}{\mu_w} \left( \omega - \alpha A_1 - \alpha \frac{\mu_w}{\mu} A_2 Y \right) \frac{d^2\Phi}{dY^2} = 0, \quad (3.24)$$

$$Y \rightarrow \infty, \quad \Phi = C \left[ \pm \frac{\alpha}{A_2} - \frac{\mu}{\mu_w} \left( \frac{\omega}{\alpha} - u_0 \right) \right] C A_2 Y \quad (3.25)$$

(the plus or minus sign in front of the first term inside the brackets corresponds to  $\alpha_r$  positive or negative, respectively), at the interface between the film and the lower deck of the air stream,  $Y = y = 0$

$$\Phi = \Psi, \quad (3.26)$$

$$\frac{d\Psi}{dy} = H_0^2 \hbar A_3 \left( \frac{\mu_w}{\mu} - 1 \right) + \frac{d\Phi}{dY}, \quad (3.27)$$

$$\frac{d^2\Phi}{dY^2} = \frac{\mu_w}{\mu} \frac{d^2\Psi}{dy^2}, \quad (3.28)$$

$$\hbar[\omega - \alpha A_1] - \alpha \frac{\Psi}{H_0} = 0, \quad (3.29)$$

$$\begin{aligned} \frac{d^3\Psi}{dy^3} = & -iH_0 \left( \frac{\mu}{\mu_w} \right)^2 \left[ (\omega - \alpha A_1) \left( \frac{\rho_w}{\rho} \frac{d\Psi}{dy} - \frac{d\Phi}{dY} \right) + \alpha A_2 \left( \frac{\rho_w}{\rho} \Psi - \frac{\mu_w}{\mu} \Phi \right) \right] \\ & + iH_0 \left( \frac{\mu}{\mu_w} \right)^2 \left[ \hbar \alpha H_0^2 \frac{1}{Fr} \left( \frac{\rho_w}{\rho} - 1 \right) + \hbar \frac{1}{We} \alpha^3 \right] + \frac{\mu}{\mu_w} \frac{d^3\Phi}{dY^3}, \end{aligned} \quad (3.30)$$

and in the liquid film

$$\frac{d^4\Psi}{dY^4} + iH_0 \left( \frac{\mu}{\mu_w} \right)^2 \frac{\rho_w}{\rho} (\omega - \alpha A_1 - \alpha A_2 y) \frac{d^2\Psi}{dY^2} = 0, \quad (3.31)$$

$$y = -1, \quad \Psi = \frac{d\Psi}{dy} = 0, \quad (3.32)$$

with

$$\left. \begin{aligned} Fr = \frac{u_f^2}{gH_f}, \quad We = \frac{\rho u_f^2 H_f}{\sigma \varepsilon^4}, \quad H_0 = H_0(x_0), \quad A_1(x_0) = u_0(y=0) = x_0^{1/4} \sqrt{0.664}, \\ A_2(x_0) = \frac{\partial u_0}{\partial y}(y=0) = x_0^{1/4} \frac{\sqrt{0.664}}{H_0(x_0)}, \quad A_3(x_0) = \frac{\partial U_0}{\partial \bar{Y}}(\bar{Y}=0) = \frac{0.332}{\sqrt{x_0}}, \end{aligned} \right\} \quad (3.33)$$

and  $Y, y$  the transformed coordinates according to (3.21). Finally,  $C$  is a constant that is related to the linearized pressure or the displacement thickness. It enters the analysis as the linearized boundary condition for the pressure, (3.11), is incorporated in the lower-deck formulation via the boundary condition at infinity for the longitudinal velocity, (3.8).

At this point it should be noted that the solution to the above linearized set of equations loses analyticity in  $\alpha$  along the imaginary axis,  $\alpha_r = 0$ . This is a result of the change in sign in the solution of the upper-deck equations depending on the sign of  $\alpha_r$  and is reflected in the boundary condition at infinity (3.25). Consequently, the

analysis that follows is restricted to positive values of the real part of the wavenumber  $\alpha$ , which will anyway be positive for real signals (see also Huerre & Monkewitz 1985).

## 4. Method of solution

### 4.1. Eigenvalue calculation

The linearized set of equations presented in the previous section can be solved to provide the dispersion relation of the system,  $D(\omega, \alpha; x_0, Fr, We, \rho/\rho_w, \mu/\mu_w) = 0$ , with both  $\omega$  and  $\alpha$  treated as complex variables and the density ratio,  $\rho/\rho_w$ , the viscosity ratio,  $\mu/\mu_w$ , the Froude number,  $Fr$ , the Weber number,  $We$ , and the streamwise station  $x_0$  where the disturbance is applied, as parameters of the problem. There is normally a large number of eigenvalues associated with a certain set of parameter values. Since we are interested in identifying the most unstable eigenmode for the air–water system and for two different families of eigenvalues, corresponding to TS and interfacial waves, we initially obtain an asymptotic solution for the eigenfrequency in terms of the wavenumber taken as real, or vice versa. Normally, it is easier to solve asymptotically in terms of  $\omega$ ; the asymptotic results are given in the next section. Then, a numerical scheme is used in order to provide a solution for  $\omega$ , in terms of  $\alpha$  and the rest of the parameters of the problem. Finally the parameter values are advanced and the evolution of  $\omega$  in the parameter space is traced by means of a simple continuation procedure. The numerical procedure that gives  $\omega$  or  $\alpha$ , given the rest of the problem parameters, is described in the following. First, the stream function,  $\Phi$ , is transformed,

$$\hat{\Phi} = \Phi - C \left[ \frac{\alpha}{A_2} - \frac{\mu}{\mu_w} \left( \frac{\omega}{\alpha} - A_1 \right) \right] + CA_2 Y \quad (4.1)$$

so that  $\hat{\Phi}$  approaches zero exponentially fast as  $Y$  goes to infinity. Furthermore, two new variables are introduced,  $S = d^2\hat{\Phi}/dY^2$ ,  $R = d^2\Psi/dy^2$ , such that  $R(y = -1) = 1$  as a condition that normalizes the eigenvector. Then we calculate, through asymptotic analysis, a certain value for the frequency  $\omega$  and the quantity

$$C_2 \equiv \frac{d^3\Psi}{dy^3} - \frac{\mu}{\mu_w} \frac{d^3\Phi}{dY^3} = -iH_0 \left( \frac{\mu}{\mu_w} \right)^2 \left[ (\omega - \alpha A_1) \frac{d\Psi}{dy} \left( \frac{\rho_w}{\rho} - 1 \right) + \alpha A_2 \Psi \left( \frac{\rho_w}{\rho} - \frac{\mu_w}{\mu} \right) \right] \\ + iH_0 \left( \frac{\mu}{\mu_w} \right)^2 \hbar \left[ \alpha H_0^2 \frac{1}{Fr} \left( \frac{\rho_w}{\rho} - 1 \right) + \alpha^3 \frac{1}{We} - (\omega - \alpha A_1) H_0^2 A_3 \left( \frac{\mu_w}{\mu} - 1 \right) \right] \quad (4.2)$$

which is obtained from (3.30); boundary conditions (3.26) and (3.27) have been incorporated in the right-hand side of this expression. In this fashion, we obtain the following set of equations to be solved:

$$\frac{d^2 S}{dY^2} + iH_0 \frac{\mu}{\mu_w} \left( \omega - \alpha A_1 - \alpha \frac{\mu_w}{\mu} A_2 Y \right) S = 0, \quad (4.3)$$

$$Y \rightarrow \infty, \quad S \rightarrow 0, \quad (4.4)$$

$$Y = 0, \quad S = \frac{\mu_w}{\mu} R, \quad \frac{dR}{dy} - \frac{\mu}{\mu_w} \frac{dS}{dY} = C_2, \quad (4.5)$$

$$\frac{d^2 R}{dY^2} + iH_0 \left( \frac{\mu}{\mu_w} \right)^2 \frac{\rho_w}{\rho} (\omega - \alpha A_1 - \alpha A_2 y) R = 0, \quad (4.6)$$

$$y = -1, \quad R = 1. \quad (4.7)$$

This set of equations can now be solved for  $S$  and  $R$ , assuming values for  $C_2$ ,  $\hbar$ ,  $C$ ,  $\omega$ , using the method of finite elements with increased accuracy owing to the reduction in the order of differentiation. More specifically the  $B$ -cubic splines are used as basis functions, which guarantee continuity up to the second-order derivative of the unknown function. For more details on the application of  $B$ -cubic splines in the finite element method the interested reader is referred to the article by Pelekasis, Tsamopoulos & Manolis (1992). Having solved for  $R$  and  $S$  the remaining unknowns,  $C_2$ ,  $\hbar$ ,  $C$ ,  $\omega$ , can be calculated via equations (4.2) and (3.29), and (3.26) and (3.27), after they are transformed according to (4.1):

$$\hat{\Phi}(Y = 0) + C \left[ \frac{\alpha}{A_2} - \frac{\mu}{\mu_w} \left( \frac{\omega}{\alpha} - A_1 \right) \right] = \Psi(y = 0), \quad (4.8)$$

$$\frac{d\Psi}{dy}(y = 0) = H_0^2 \hbar A_3 \left( \frac{\mu_w}{\mu} - 1 \right) + \frac{d\hat{\Phi}}{dY}(Y = 0) + CA_2. \quad (4.9)$$

In order to determine all the terms in these four equations the values of  $\hat{\Phi}$ ,  $d\hat{\Phi}/dY$ ,  $\Psi$ ,  $d\Psi/dy$  at  $Y = y = 0$  are needed. These can be calculated, given the functions  $S$  and  $R$ , via the following relations:

$$\hat{\Phi}(Y = 0) = \int_{\infty}^{Y=0} dt(SY - St), \quad \frac{d\hat{\Phi}}{dY}(Y = 0) = \int_{\infty}^{Y=0} S dt, \quad (4.10)$$

$$\Psi(y = 0) = \int_{-1}^{y=0} dt(Ry - Rt), \quad \frac{d\Psi}{dy}(y = 0) = \int_{-1}^{y=0} R dt, \quad (4.11)$$

where use has been made of the boundary conditions

$$\Psi(y = -1) = \frac{d\Psi}{dy}(y = -1) = 0, \quad \hat{\Phi}(Y \rightarrow \infty) = \frac{d\hat{\Phi}}{dY}(Y \rightarrow \infty) = 0. \quad (4.12)$$

Once  $\omega$  and  $C_2$  have been updated, (4.3)–(4.7) are solved again and the entire procedure is repeated until convergence. Unfortunately this algorithm does not converge in the range of interest of the parameters of the problem. Consequently, an alternative approach via the more powerful Newton's method is adopted. The same set of equations is solved, with the difference that at each iteration one obtains a new value for all the unknowns simultaneously. This requires a reliable initial guess, which is provided by the previous method. Then simple continuation is used to advance the solution in the parameter space with Newton's method. Normally three to four iterations are sufficient to give accuracy up to the eighth significant digit. The accuracy of the spatial discretization is determined by the number of elements used in each phase. Normally 50 elements are used in the liquid and 200 elements in the gas phase. This is enough to provide accuracy of the eigenvalues up to, at least, the third significant digit. Despite the fact that when Newton's iterations are used the Jacobian matrix is full owing to the integrals in (4.10), (4.11), as opposed to being banded in the case of successive iterations, the CPU time required for the calculations is smaller owing to the much smaller number of iterations that is required for convergence.

Once temporal stability analysis has been completed, the calculation is repeated with the wavenumber  $\alpha$  treated as an unknown. It is not very difficult to solve for  $\alpha$  because it turns out that neutrally stable points in the temporal case,  $\omega_i = 0$ , are also neutrally stable points in the spatial case,  $\alpha_i = 0$ . In addition, it is found that Gaster's

transformation which was originally discovered for TS waves in a single fluid (Gaster 1962), holds in our problem as well for both families of eigenvalues. More specifically, it is found that  $\alpha_i \approx -\alpha_r \omega_i / \omega_r$  in a substantial region around the neutrally stable points. As a result it is possible to obtain a solution for  $\alpha$  complex in terms of  $\omega$  in the vicinity of a neutral point for  $\alpha_r$  using an initial guess for  $\alpha_i$  provided by the above relationship. Subsequently, it is easy to cover the entire parameter space for both families of eigenmodes, treating  $\alpha$  as an unknown.

An important issue can be raised regarding the parameter continuation procedure: it is not entirely certain whether the eigenvalues that are obtained numerically with the above procedure remain the most dangerous ones, as the continuation in the parameter space proceeds, among the rest of the eigenvalues in the spectrum. In order to resolve this issue the entire spectrum of eigenvalues is calculated occasionally, given  $\alpha$  for temporal or  $\omega$  for spatial analysis along with the rest of the parameters, via solution of the eigenvalue problem defined by the above set of equations. A minor complication arises in the computation of  $\alpha$  in spatial analysis owing to the nonlinear dependence on  $\alpha$  of equations (4.2) and (4.8). This is resolved by introducing the additional unknowns and equations  $C^* = \alpha C$ ,  $\tilde{h}^* = \alpha \tilde{h}$ ,  $\tilde{h}^{**} = \alpha \tilde{h}^*$ , that depend linearly on  $\alpha$ . Discretizing (4.2) and (4.6) in the fashion described above we obtain the generalized eigenvalue problem,

$$\mathbf{A}x + \gamma \mathbf{B}x = 0, \quad (4.13)$$

where  $\gamma$  stands for either  $\omega$  or  $\alpha$ ,  $x$  is the eigenvector and  $\mathbf{A}$ ,  $\mathbf{B}$ , are matrices incorporating the finite element discretization and the parameters of the problem. A standard IMSL routine dedicated to the treatment of generalized complex eigenvalue problems is employed for the solution of (4.13). This approach verified that the eigenvalues already obtained via parametric continuation are indeed the most unstable eigenvalues of their corresponding families. Details of the computations are not given here in the interest of brevity.

#### 4.2. 'Pinching' method

A central aspect of the numerical solution is the application of the 'pinching' method for the determination of the convective or absolute character of the unstable waves that develop in response to an impulsive disturbance of the flow at some station  $x_0$ . It was originally proposed by Briggs (1964) and Bers (1975) in the context of plasma physics and has recently been extensively used in fluid dynamics as well, Huerre & Monkewitz (1985, 1990). This method consists of two steps both involving solution of the dispersion relation, which is provided implicitly by the solution of the linearized set of equations given in the previous section. First, the frequency  $\omega$  is obtained as a function of  $\alpha$ , taken to be real. If a certain range of positive values for  $\omega_i$  is identified, then unstable waves exist. Their specific nature is determined in the next step which involves solution for the wavenumber  $\alpha$ , taken as complex, as a function of  $\omega = \omega_r + i\omega_i$ . The goal is to find the complex value of  $\alpha_0$  for which a wave with zero group velocity is obtained,  $(d\omega/d\alpha)(\alpha_0) = 0$ . The complex frequency  $\omega_0 = \omega(\alpha_0)$  is called the absolute frequency and normally corresponds to a second-order algebraic branch point of the function  $\alpha(\omega)$ . In order for the two branches  $\alpha^-(\omega)$ ,  $\alpha^+(\omega)$  to actually represent left- and right-moving waves when the inverse Laplace transform is taken, hence establishing that the 'pinching' point indeed signifies a convectively/absolutely unstable family, they must be located on different semiplanes, defined by the real  $\alpha$ -axis, as their contour deforms or, equivalently, as  $\omega_i$  increases (Lingwood 1997). Then, the complex frequency  $\omega_0 = \omega(\alpha_0)$  that is obtained

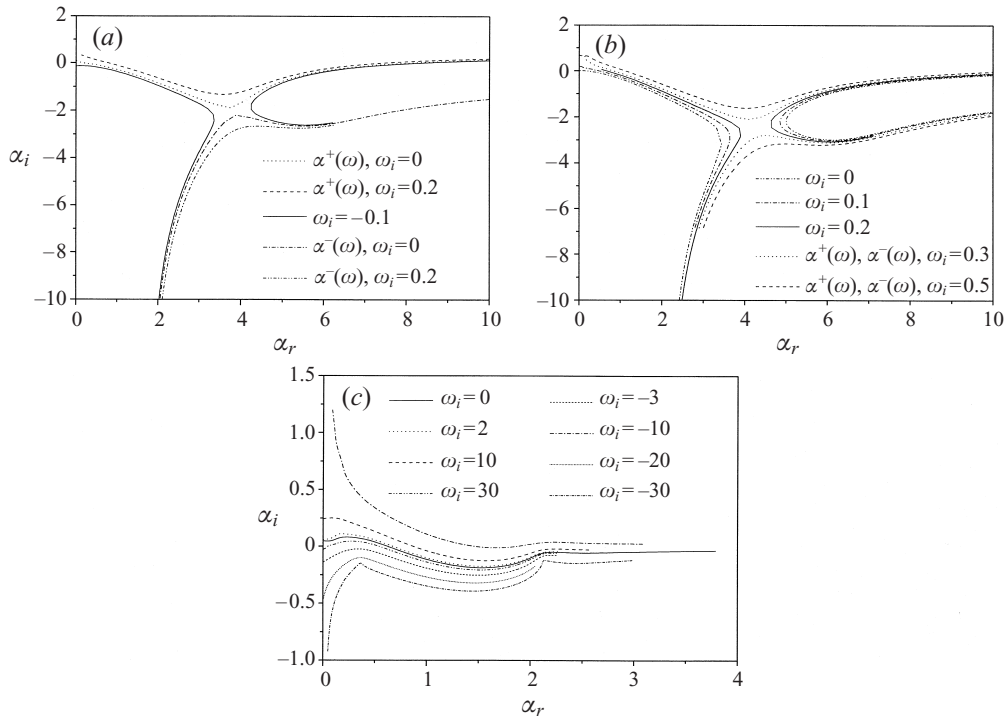


FIGURE 3. 'Pinching' diagram of the air–water system when (a)  $x_0 = 0.6$ , (b)  $x_0 = 1.0$ , for the interfacial mode and when (c)  $x_0 = 1$ , for the TS mode, where only the  $\alpha^+(\omega)$  branch is shown;  $We^{-1} \approx 66$ ,  $Fr \approx 30$ .

at the pinching point provides the growth rate of a wave packet that always remains in the neighbourhood of the point  $x_0$  where the impulse was originally applied. Consequently, solving for  $\alpha$  as a function of  $\omega_r$  for different values of  $\omega_i$  amounts to deforming the contour of the two spatial branches  $\alpha^-(\omega)$ ,  $\alpha^+(\omega)$ . For some value of  $\omega_i = \omega_{i0}$  the two branches become pinched, figure 3. Pinching occurs precisely at the point where the group velocity is zero. The Briggs criterion identifies as convectively unstable waves those for which  $\omega_{i0} < 0$ , whereas waves for which  $\omega_{i0} > 0$  are absolutely unstable. The former waves evolve in space whereas the latter evolve in time at a certain spatial location (see also the schematic representations available in Huerre & Monkewitz 1990).

As can be seen from figure 3(a, b) and has been extensively verified for a wide range of parameters in the present study, this is the case with interfacial waves whenever they are identified as convectively/absolutely unstable. As will be seen in the next section, interfacial waves are convectively unstable except for a region in  $x_0$  in which they are absolutely unstable. For example when  $\rho/\rho_w \approx 0.001$ ,  $\mu/\mu_w \approx 0.018$ ,  $Fr \approx 30$ ,  $We^{-1} \approx 66$ , the interfacial waves for the air–water system are convectively unstable except for a pocket of absolute instability,  $0.7 \leq x_0 \leq 2.5$ . Figure 3(a, b) shows the pinching process for the above parameter values when  $x_0$  is 0.6 and 1.0. Note that pinching occurs when  $-0.1 \leq \omega_i \leq 0$  in the former case whereas  $0.2 \leq \omega_i \leq 0.3$  in the latter and that the two branches move towards a different semi-plane as  $\omega_i$  increases.

On the other hand, TS waves are convectively unstable since no pinching point was found for the entire parameter range that is relevant to our problem; see also figure 3(c) where only one branch is shown. It should be noted that 'non-pinching'

branch points exist, as can be inferred by noticing the two ‘kinks’ that start developing for large negative values of  $\omega_i$  in figure 3(c). These kinks probably correspond to branch points between the basic mode shown in figure 3(c) and higher TS eigenmodes (Hultgren 1987). However, such branch points are non-pinching because all these branches remain on the same semi-plane as  $\omega_i$  increases. Branches corresponding to higher TS eigenmodes were identified numerically in the present study also. However, the specific process by which they pinch with the leading TS branch was not pursued. In addition, on comparing the numerical findings for TS waves of the air–water system examined here with the results for a single-phase boundary layer flowing past a flat plate we find that they are almost indistinguishable owing to the very small value of the density and viscosity ratios. In fact, TS waves in a boundary layer over a flat plate are known to be spatially growing (Gaster 1965) in the presence of an impulsive disturbance. This, in conjunction with our own findings, leads to the conclusion that TS waves remain convectively unstable in the context of our study as well.

The response of convectively unstable flows to a disturbance with constant frequency  $\omega_f$  applied at a station  $x_0$  of the basic flow (the signalling problem) is determined by the findings of spatial analysis. That is, setting  $\omega$  real,  $\omega = \omega_f$ , the asymptotic behaviour of the system as  $t \rightarrow \infty$  is time periodic with frequency  $\omega_f$  and wavenumber  $\alpha = \alpha_r + i\alpha_i$  provided by the solution of the dispersion relation with  $\alpha$  unknown (Huerre & Monkewitz 1985). Therefore, in the following section in regions where both families of waves are convectively unstable we use their spatial growth rate,  $\alpha_i$ , in order to determine which one of the two will dominate the flow locally. In regions where interfacial waves are found to be absolutely unstable they will eventually dominate the flow locally.

As was mentioned in the previous paragraphs the evaluation of the pinching points was originally made by constructing the two branches  $\alpha^-(\omega)$ ,  $\alpha^+(\omega)$ , while parametrically varying  $\omega_r$  for different values of  $\omega_i$ . Thus, it is verified that the two branches reside in different semiplanes of the complex plane as  $\omega_i$  increases; the pinching diagram is constructed and the location of the pinching point is identified by noting the interval of values of  $\omega_i$  within which the mutual exchange between the two branches takes place. Clearly, this method cannot give the pinching point with great accuracy. It provides, however, a good first estimate,  $\omega_{0,ap}$ ,  $\alpha_{0,ap}$ , for a more systematic search. To this end, we use the pinching condition  $(d\omega/d\alpha)(\alpha_0) = 0$  or  $(\partial\omega_r/\partial\alpha_r) + i(\partial\omega_i/\partial\alpha_r) = 0$ , upon introducing complex differentiation. In this fashion the pinching point is obtained as the point  $\alpha = \alpha_r + i\alpha_i$  in the  $\alpha$  complex plane which minimizes the function  $F(\alpha_r, \alpha_i) = (\partial\omega_r/\partial\alpha_r)^2 + (\partial\omega_i/\partial\alpha_r)^2$ . Clearly, the point  $\alpha_0(\omega_0)$  in the neighbourhood of  $\alpha_{0,ap}(\omega_{0,ap})$ , which minimizes  $F(\alpha_r, \alpha_i)$  with  $F(\alpha_{0r}, \alpha_{0i}) \approx 0$  corresponds to the pinching point. This can be easily verified by calculating the two branches corresponding to  $\omega_{0i}$ . The complex frequency  $\omega = \omega_r + i\omega_i$  can be calculated as a function of the complex wavenumber  $\alpha$  numerically, as was shown in §4.1. At the same time, analytical evaluation of the partial derivatives appearing in  $F$  is not straightforward. Therefore, we resort to numerical differentiation, introducing a small parameter  $\delta_D$  and approximating  $F$  as

$$F(\alpha_r, \alpha_i) = \left( \frac{\omega_r(\alpha_r + \delta_D, \alpha_i) - \omega_r(\alpha_r, \alpha_i)}{\delta_D} \right)^2 + \left( \frac{\omega_i(\alpha_r + \delta_D, \alpha_i) - \omega_i(\alpha_r, \alpha_i)}{\delta_D} \right)^2. \quad (4.14)$$

It is understood that the minimum should not vary as  $\delta_D \rightarrow 0$ , and indeed this was verified to be the case. In this fashion, using a standard minimization routine, the pinching point was calculated within two to three significant digit accuracy. In

particular, for the cases depicted in figures 3(a) and 3(b) it was found that  $\omega_{0i} = -0.011$  and 0.250, respectively.

## 5. Results and discussion

### 5.1. Temporal and spatial stability analysis

We are primarily interested in the study of the stability of the air–water system. In this case, for a gas layer with large free-stream velocity,  $U_\infty = 40 \text{ m s}^{-1}$ , that flows over a plate with characteristic length  $L = 30 \text{ cm}$ , which is well within the range of chord lengths of wing sections used in airfoil testing (Thomson, Jang & Dion 1995), and under mild rainfall conditions,  $\dot{r} = 100 \text{ mm h}^{-1}$ , the Reynolds number takes the value  $Re = 8 \times 10^5$ , and the fastest growing TS mode is the one with wavelength  $\lambda = LRe^{-3/8} = 2 \text{ mm}$  (Smith 1979). The rest of the parameters take the values,  $\mu/\mu_w \approx 0.018$ ,  $\rho/\rho_w \approx 0.001$ ,  $Fr \approx 30$ ,  $We^{-1} \approx 66$ . Keeping the rest of the parameter values constant, we find that the length  $L^*$  for which the condition  $H_f(L^*)/L^*Re^{-5/8}(L^*) = 1$  is satisfied is, roughly, 30 cm. This being comparable in magnitude with the length of wing sections used in wind tunnel testing of airfoils, and given the very high value of the Reynolds number, we can assume that we will be operating in the triple-deck regime. Despite the fact that we have ignored higher-order corrections in the small parameter  $Re^{-1/8}$ , the theory gives a fairly good qualitative picture of the flow for the range of Reynolds numbers examined here; see also figure 1 in Healey (1995) for a comparison between experimental data, the leading-order triple-deck prediction and the solution of the Orr–Sommerfeld stability equations for the neutral stability curve of the flat boundary layer. In this case the characteristic film thickness as given by (2.13),  $H_f \approx 0.06 \text{ mm}$ , is also of the order of magnitude of measured heights for films that form on airfoils (Feo & Gonzalez 1988) under simulated rainfall conditions.

The streamwise station on the plate,  $x_0$ , where the disturbance is applied is an additional parameter that takes the value 1 when  $x'_0 \approx 30 \text{ cm}$ , for the above set of parameter values. However,  $x_0$  can also take values that are larger than 1, as long as  $x_0 = O(1)$  so that the assumption that the film thickness,  $H_f$ , and the lower-deck thickness,  $LRe^{-5/8}$ , are comparable in size is not violated. In general, the idea is that given the free-stream velocity and the rainfall rate one can calculate the length  $L^*$  for the air–water system for which  $H_f(L^*)/L^*Re^{-5/8}(L^*) = 1$ . Then, given the length of the plate, approximating the chord length of the wing section under consideration, the relevant range of dimensionless streamwise locations,  $x_0$ , is calculated. For example, for the above parameter range if a plate of length 70 cm was used instead, then, since  $L^*$  is 30 cm,  $x_0$  can be as high as 7/3.

#### 5.1.1. Tollmien–Schlichting waves

In this parameter range we focus on two possible limiting structures in the flow. According to the first one the film is so heavy and viscous that it behaves almost like a solid. Interfacial waves occur as a higher-order effect, dominated by the TS waves that develop inside the gas phase in a fashion similar to flow past a dry flat plate. Consequently, and provided that the wavenumber  $\alpha$  remains  $O(1)$  as  $\mu/\mu_w \rightarrow 0$ , the stability equations inside the gas phase collapse to those obtained by Smith (1979) who applied triple-deck theory to flow past a dry flat plate. Setting  $\bar{\Phi} = \Phi(\mu/\mu_w)$ ,

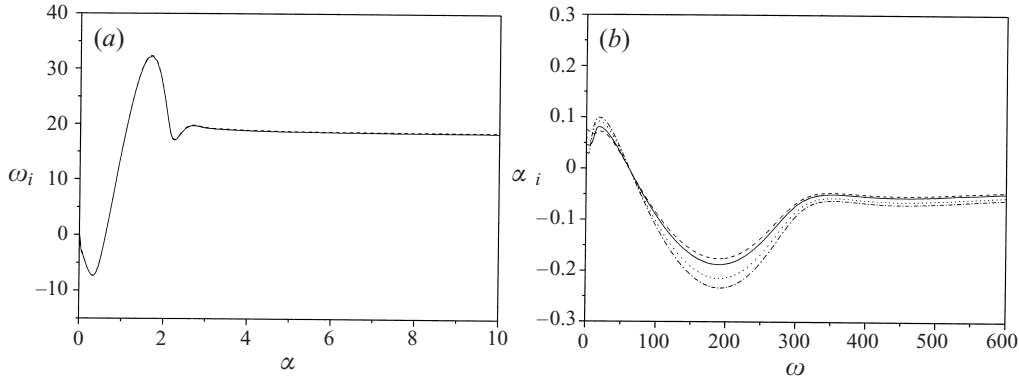


FIGURE 4. (a) Evolution of the growth rate,  $\omega_i$ , as a function of the wavenumber,  $\alpha$ , for the TS mode: —, numerical solution obtained for the air–water system,  $\mu/\mu_w = 0.018$ ; - - -, asymptotic prediction in the limit  $\mu/\mu_w \rightarrow 0$ ;  $We^{-1} \approx 66$ ,  $Fr \approx 30$ . (b) Evolution of the growth rate,  $\alpha_i$ , as a function of the frequency,  $\omega$ , for the TS mode at various streamwise locations ( $\omega_i = 0$ ,  $We^{-1} \approx 66$ ,  $Fr \approx 30$ ): —,  $x_0 = 1.0$ ; - - -,  $x_0 = 0.6$ ; ····,  $x_0 = 3.0$ ; -·-·-,  $x_0 = 6.0$ .

$\bar{\omega} = \omega(\mu/\mu_w)$ , and satisfying no slip at the interface we obtain  $\bar{\omega}$  as the solution of

$$\frac{d\text{Ai}}{dz} + \frac{(H_0\alpha A_2)^{1/3}}{(A_2)^2} i^{1/3} \alpha \int_{\infty}^z \text{Ai} dt = 0, \quad z = -\frac{H_0\bar{\omega}i^{1/3}}{(H_0\alpha A_2)^{2/3}}, \quad (5.1)$$

with Ai the Airy function of the first kind. By substituting  $H_0$ ,  $A_2$ , as functions of  $x_0$  and transforming  $\alpha$  according to  $\alpha/H_0 = k$ , equation (5.1) gives the equation derived by Smith (1979). Solving (5.1) for the neutral stability values of  $\omega$  and  $\alpha$  one obtains

$$\alpha = x_0^{1/8} 0.332^{3/4} \sqrt{2}, \quad \bar{\omega} \approx 1.079. \quad (5.2)$$

The above equations predict that when  $x_0 = 1$  the value of  $\alpha$  for which neutral stability is obtained is 0.618, a result verified by the numerical results in the present study, see figure 4(a). It is also easily seen that the same result holds when  $\mu/\mu_w = 1$  or  $\mu/\mu_w \rightarrow 0$  with  $\alpha = O(1)$ . It will be seen later that the lower neutral curve of the TS waves is recovered, and that the neutral stability curve for the air–water system closely follows equation (5.2).

Simple numerical continuation, as described in the previous section, is then used to march the solution to the parameter range of interest. An extensive numerical study has been conducted in order to identify the stability characteristics of this solution family, first in the context of temporal stability. Most of the parameter space has been covered, but results are presented for the parameter range relevant to the problem at hand. As can be seen from figure 4(a) the dependence of  $\omega_i$  on the wavenumber  $\alpha$  for the temporal TS family closely resembles the findings of single-phase stability analysis. Gravitational and capillary forces are not big enough to affect the stability characteristics of the system significantly. Note the  $(\mu/\mu_w)^2$  term that multiplies the inverse Weber number,  $We^{-1}$ , and the inverse Froude number,  $Fr^{-1}$ , in equation (4.2), as opposed to the large values reached by  $\omega$  when  $\alpha$  remains  $O(1)$  in the context of TS waves. The viscosity and density ratios are very small for the air–water system so, unless  $We^{-1}$  or  $Fr^{-1}$  is quite large, they cannot play an important role. Thus, the family is stable for very long waves, whereas it exhibits a maximum in the growth rate at moderate values of the wavenumber,  $\alpha \approx 1.5$ , remaining unstable for the entire range of short wavelengths. This behaviour indicates that the family of TS waves that

is calculated here is part of the lower neutral branch in the fully stability diagram; see also figure 1 in Smith (1979). In figure 4(b) the evolution of the family of spatial TS waves is given as the location of the base flow,  $x_0$ , varies. It is seen that the value of the real frequency,  $\omega$ , for which the growth rate,  $\alpha_i$ , crosses to negative values does not depend on  $x_0$ , whereas the wavenumber,  $\alpha$ , increases like  $x_0^{1/8}$ . This behaviour persists for the values of the frequency and wavenumber corresponding to the maximum, in absolute value, of  $\omega_i$ . This agrees well with the result presented by Smith (1979), after applying the proper transformation for the wavenumber and eigenfrequency between that study and the present one for the leading-order behaviour of the lower neutral branch of the TS waves, as expressed through (5.2).

5.1.2. Interfacial waves

It is also known that when a more viscous fluid is sheared by a less viscous one a long-wave interfacial instability arises, Yih (1967), Hooper & Boyd (1987). The context of the last two studies is different from that of the present one, since the first one treats channel flow, whereas the second one considers the thickness of the viscous sub-layer in the less viscous fluid to be much larger than the thickness of the viscous film that is attached on the plate. An interesting limiting structure was presented by Timoshin (1997), in which the streamwise velocity and shear rate at the interface remain finite in the limit  $\mu/\mu_w \rightarrow 0$ . In this limit and in the context of the non-dimensionalization used here the eigenfrequency of the interfacial mode is

$$\omega = \alpha u_0 - \frac{i\alpha^4}{3} \bar{W}e^{-1} - \frac{iH_0^2 \alpha^2 (\rho_w/\rho) - 1}{3 \bar{F}r} + H_0 \frac{\alpha^2}{2} A_3 \frac{-\text{Ai}(0)D^{2/3} + \frac{2}{3} (d\text{Ai}/dz)(0)D}{\pm A_3^2 (d\text{Ai}/dz)(0) + \alpha D^{1/3} \int_{\infty}^0 \text{Ai} dz}$$

$$D = (iH_0 \alpha A_2), \quad \bar{W}e = We \left( \frac{\mu_w}{\mu} \right)^2, \quad \bar{F}r = Fr \left( \frac{\mu_w}{\mu} \right)^2, \quad \int_{\infty}^0 \text{Ai} dz = -\frac{1}{3}, \quad \pm : \alpha_r \geq 0$$

(5.3)

where dependence on the ratio  $\mu/\mu_w$  has been scaled out of  $\bar{W}e, \bar{F}r$ . Simple numerical continuation was used, as described in the previous section, between this asymptotic solution and the dimensionless parameter range of interest in the present study. Figure 5 shows the behaviour of the family corresponding to interfacial waves for the same parameter values that were used for the calculations in figure 4(a), as predicted by the asymptotic relation (5.3) and computed numerically via solution of the eigenvalue problem defined in §4.1. The stability analysis presented by Tsao *et al.* (1997) essentially covers the same asymptotic limit as (5.3). As can be seen from figure 5 this limit significantly shrinks the range of unstable wavenumbers by more than halving the neutral stability limit, which is bound to have an effect on the spatio-temporal properties of interfacial waves. Now long waves are unstable, the maximum growth rate is predicted for larger values of the wavenumber,  $\alpha \approx 5$ , while short waves become stable. This is in contrast to the situation observed for TS waves where the family is stable as  $\alpha \rightarrow 0$ . Consequently it is conjectured that this family is part of the upper neutral branch of the full stability diagram; see figure 13 in Yiantsios & Higgins (1988) for the neutral stability diagram of the interfacial mode for a different parameter range. The stabilizing effect that surface tension and gravity normally have for this type of wave is encountered here as well. Comparing the growth rates of these two families it follows that TS waves grow much faster than interfacial waves. This is contrary to what Timoshin (1997) found in his study, when operating, however, in the regime of relatively short waves with density ratio of order

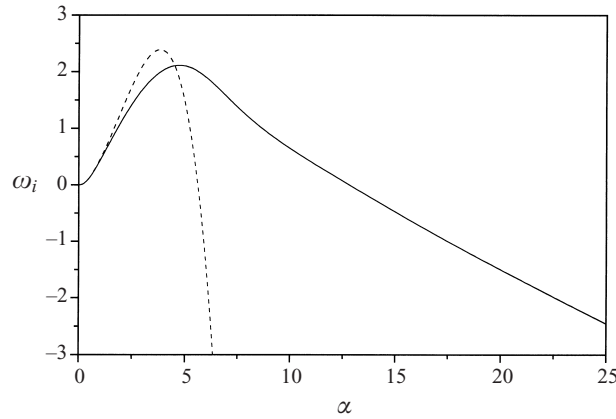


FIGURE 5. Evolution of the growth rate,  $\omega_i$ , as a function of the wavenumber,  $\alpha$ , for the interfacial mode: —, numerical solution obtained for the air–water system,  $\mu/\mu_w = 0.018$ ; - - -, asymptotic prediction in the limit  $\mu/\mu_w \rightarrow 0$ ;  $We^{-1} \approx 66$ ,  $Fr \approx 30$ .

one. Clearly, the air–water system does not belong to this regime. Our results are in agreement with the findings of Boelens & Hoeijmakers (1997), and Ozgen *et al.* (1998), who performed a temporal stability analysis on Newtonian or non-Newtonian de-/anti-icing fluids, sheared into motion by an air stream forming a boundary layer on top of them, and found that TS waves dominate interfacial waves.

Contrary to the findings of temporal analysis, a more thorough study of the dispersion relation, treating both  $\omega$  and  $\alpha$  as complex numbers, reveals that the interfacial waves of the air–water system exhibit a pocket of absolute instability,  $0.7 \leq x_0 \leq 2.5$  when  $Fr \approx 30$ ,  $We^{-1} \approx 66$ , in response to an impulsive disturbance. Table 1 shows the evolution of the imaginary part  $\omega_{0i}$  of the algebraic branch point, also known as the absolute frequency, and the maximum in  $\omega_i$  predicted by temporal analysis as a function of the streamwise location of the disturbance  $x_0$ , indicating a region of absolute instability. Indicative pinching diagrams are shown in figures 3(*a, b*) and 6(*a, b*) when  $x_0 = 0.6, 1, 1.5, 3.0$ , respectively, with the imaginary part of the branch point  $\omega_0$  changing sign from negative to positive in the interval  $0.6 < x_0 < 0.7$  and vice versa in the interval  $2.5 < x_0 < 2.6$ . Only the general trends of the two branches to pinch and occupy different parts of the complex plane as  $\omega_i$  increases are shown in these graphs while the exact values of the pinching points are given in table 1. On the other hand TS waves are convectively unstable for the entire range of values of  $x_0$  examined. Figure 3(*c*) shows an indicative pinching diagram for TS waves when  $x_0 = 1$ . As a result interfacial waves will tend to eventually dominate the dynamic behaviour of the system within the above region. The fact that absolute instability prevails in a finite region along the plate leads to the plausible conjecture that the air–water system may exhibit self-excited global modes at specific complex frequencies,  $\omega_G$ , see also Huerre & Monkewitz (1990). This is a very important finding as it may explain the strong interaction between the film and the boundary layer that was conjectured to cause premature separation.

Outside that region of absolute instability both families are convectively unstable and their response to an isolated signal of constant frequency,  $\omega_f$ , is steady periodic, characterized by the real frequency  $\omega_f$  and by a wavenumber  $\alpha_r$  and growth rate  $\alpha_i$  determined by spatial analysis. Figure 7(*a–d*) compares the growth rates and wavelengths of the two solution families, in the context of spatial analysis, when

$x_0$	$\omega_{i,max}$	$\omega_{0,i}$
0.4	0.96	-0.253
0.6	1.45	-0.011
0.7	1.65	0.081
1.0	2.1	0.250
1.5	2.6	0.304
2.0	2.9	0.209
2.5	3.1	0.035
3.0	3.28	-0.187
5.0	3.7	-1.323
6.0	3.85	
8.0	4.0	

TABLE 1. Evolution of the maximum growth rate,  $\omega_{i,max}$ , and the absolute growth rate,  $\omega_{0,i}$ , of interfacial waves with increasing streamwise location,  $x_0$ , on the plate for the air–water system;  $\rho/\rho_w \approx 0.001$ ,  $\mu/\mu_w \approx 0.018$ ,  $Fr \approx 30$ ,  $We^{-1} \approx 66$ .

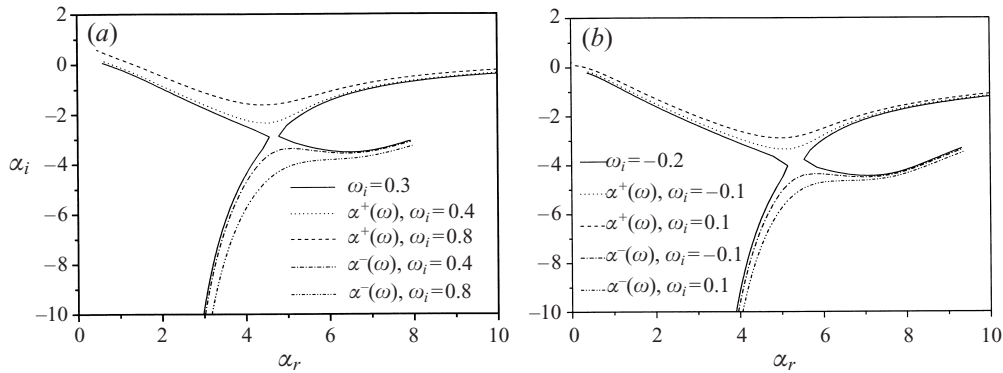


FIGURE 6. Pinching diagram of the air–water system when (a)  $x_0 = 1.5$ , (b)  $x_0 = 3.0$ , for the interfacial mode;  $We^{-1} \approx 66$ ,  $Fr \approx 30$ .

$x_0 = 0.6$  (figure 7a, b) and 3.0 (figure 7c, d) where they are both convectively unstable. It should be noted that interfacial waves have higher growth rates than TS waves, restricted, however, to a narrow range of normally lower forcing frequencies. This pattern of higher growth rates for convectively unstable interfacial waves persisted in the entire parameter range that is relevant to our study.

The curves corresponding to interfacial waves in figure 7(b, d) refer to the right-moving branch, with respect to  $x_0$ , shown in figures 3(a) and 6(b). The left going branch is the one that is gradually receding towards the lower  $\alpha$  semi-plane as  $\omega_i$  increases and it does not exhibit any spatial growth. Both branches can be obtained asymptotically in the limit  $\mu/\mu_w \rightarrow 0$ . The complex wavenumber  $\alpha$  remains  $O(1)$  when  $\omega_f = O(1)$  in this limit for right-going waves and can be obtained by solving equation (5.3) for given  $\omega = \omega_f$  real. On the other hand, the wavenumber  $\alpha$  is constantly increasing in the limit  $\mu/\mu_w \rightarrow 0$  when  $\omega_f = O(1)$  in the second branch. It can be shown that  $\alpha = \alpha_1(\mu/\mu_w)^{-6/7}$ , where  $\alpha_1$  is calculated from

$$\alpha_1^3 - \frac{H_0 A_3 (dAi/dz)(z=0)(i\alpha_0 H_0 A_2)^{2/3}}{iWe^{-1} \int_{\infty}^0 Ai dz} = 0, \quad \text{when } \frac{\mu}{\mu_w} \rightarrow 0, \quad (5.4)$$

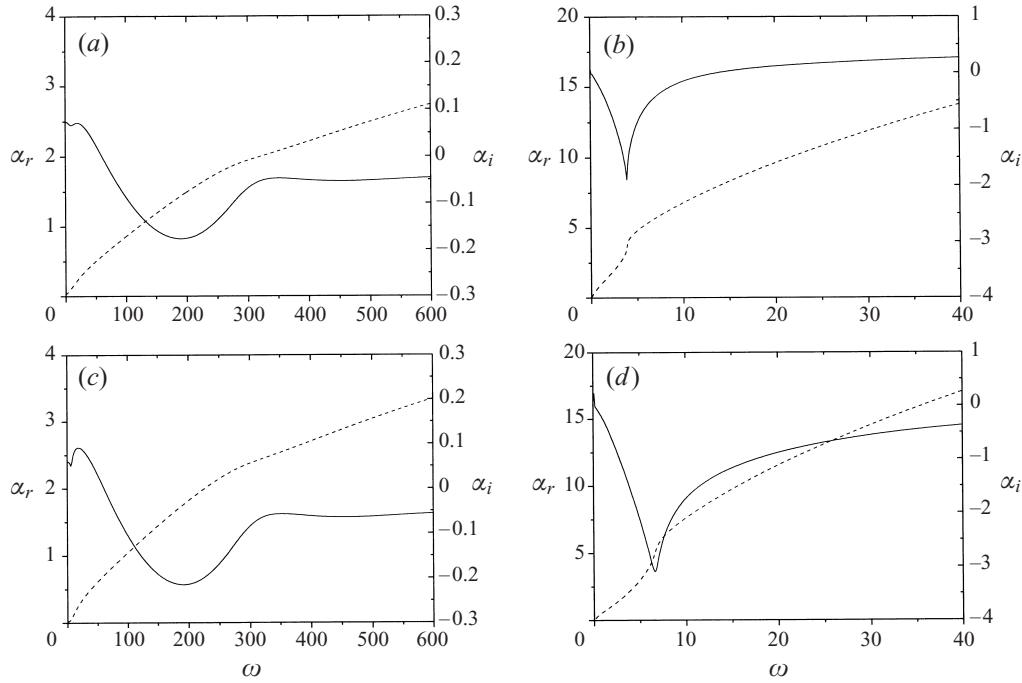


FIGURE 7. Evolution of the growth rate,  $\alpha_i$  (—), and the wavenumber,  $\alpha_r$  (- - -), as a function of the frequency,  $\omega$ , for the TS mode, (a)  $x_0 = 0.6$ , (c)  $x_0 = 3.0$  and the interfacial mode, (b)  $x_0 = 0.6$ , (d)  $x_0 = 3.0$ ;  $\omega_i = 0$ ,  $We^{-1} \approx 66$ ,  $Fr \approx 30$ .

the particular scaling arising due to the formation of an  $O(\mu/\mu_w)^{2/7}$  boundary layer, within the viscous sub-layer, which is attached to the interface. The curves corresponding to TS waves in figure 7(a,c) also represent right-moving waves and can be obtained asymptotically by the solution of (5.1) for unknown  $\alpha$ .

### 5.2. Parametric study and conclusions

An extensive parametric study has been conducted in order to identify the stability characteristics of the air–water system with varying  $Fr$  and  $We$ . As was mentioned before, the TS waves are not significantly affected by the variation of the above parameters owing to the small density and viscosity ratios between the two fluids, at least within the range of  $We$  and  $Fr$  values that is relevant to our problem. Figure 8 shows the variation of spatial growth rate  $\alpha_i$  of TS waves as a function of the wavenumber  $\alpha_r$  for different values of  $We$  and  $Fr$ . Each of these curves has been obtained by varying  $\omega_r$  while setting  $We$ ,  $Fr$ ,  $\omega_i$  and  $x_0$  fixed as is done in the construction of pinching diagrams. Owing to the convectively unstable nature of this family of waves  $\omega_i$  is set to zero while  $x_0$  is set to 1 as a reference length. Clearly, gravity and capillarity do not have any significant effect on the TS mode since all six curves are virtually indistinguishable. It was found that this behaviour persists for larger values of  $x_0$ .

Contrary to the behaviour of the TS waves, the interfacial waves are strongly affected by the variation of  $Fr$  and  $We$ . The major effect of  $We$  is that as it decreases the region of absolute instability is translated towards larger streamwise locations  $x_0$ . Increasing  $We^{-1}$  to 150 and subsequently to 350 moves the pocket of absolute instability to the interval  $1 \leq x_0 \leq 3.0$  and  $1.3 \leq x_0 \leq 3.2$ , respectively. Table 2 shows

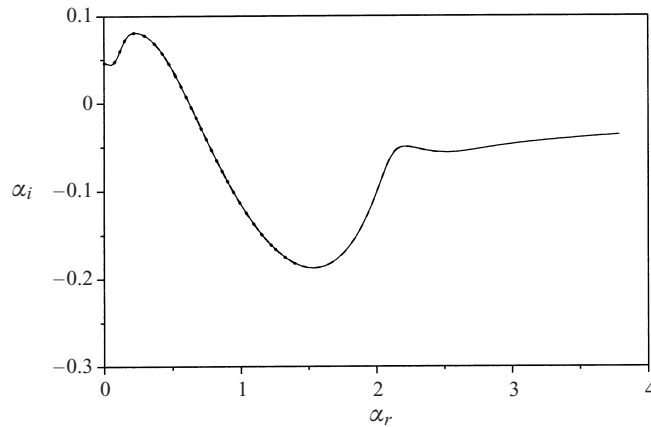


FIGURE 8. Evolution of the growth rate,  $\alpha_i$ , versus  $\alpha_r$  for the TS mode with varying  $We$  and  $Fr$ ; —,  $We^{-1} = 66$ ; - - -,  $We^{-1} = 150$ ; ·····,  $We^{-1} = 350$ ; at  $Fr \approx 30$ . —,  $Fr = 30$ ; - - -,  $Fr = 5$ ; ·····,  $Fr = 0.5$  at  $We^{-1} \approx 66$ ,  $x_0 = 1.0$ ,  $\omega_i = 0$ .

the variation of the maximum temporal growth rate,  $\omega_i$ , and the absolute growth rate,  $\omega_{0i}$ , with varying  $x_0$ , when  $We^{-1} = 350$ . Both sets of values are attenuated with respect to the ones shown in table 1 owing to the increase of  $We^{-1}$ . This behaviour persists with increasing  $We^{-1}$  until, when  $We^{-1}$  becomes of order 1000, the region of absolute instability disappears. Figure 9(a,b) shows the evolution of growth rate  $\alpha_i$  as a function of the wavenumber  $\alpha_r$  for different values of  $We^{-1}$  at two streamwise locations  $x_0 = 0.6$  and  $3.4$ ;  $\omega_i = 0$ . Near the leading edge,  $x_0 = 0.6$ , very large wavenumbers are marginally unstable and consequently surface tension does not have a noticeable effect on them, whereas small wavenumbers are not affected by surface tension. Thus, the major effect of decreasing  $We^{-1}$  is that the maximum in the growth rate, which occurs for moderate values of  $\alpha_r$ , is accentuated until pinching occurs. Indeed when  $We^{-1} \approx 30$  the family becomes absolutely unstable. On the other hand, far from the leading edge,  $x_0 = 3.4$ , short waves become increasingly unstable. As a result, increasing  $We^{-1}$  narrows the region of unstable wavenumbers by increasingly stabilizing very short waves, in favour of moderate waves which are not affected as much, thus bringing about pinching. Indeed when  $We^{-1} \approx 500$  the family becomes absolutely unstable. This can also be seen in figure 10, which shows the pinching process for the case with  $We^{-1} \approx 350$ ,  $Fr \approx 30$ ,  $x_0 = 3.0$ ; pinching occurs when  $\omega_i = 0.047$  and the family is absolutely unstable. This situation is similar to the one shown in figure 6(b) with the exception that in the latter case  $We^{-1} = 66$ , pinching occurs when  $\omega_i = -0.187$  and the family is convectively unstable.

Decreasing  $Fr$  results in narrowing the pocket of absolute instability while at the same time attenuating the maximum in the growth rate. In fact, as  $Fr$  decreases to 20 and then 15 the interval of absolute instability shrinks to  $0.7 \leq x_0 \leq 1.9$  and  $0.8 \leq x_0 \leq 1.4$ , respectively. Eventually, as  $Fr$  becomes smaller than, roughly, 10 the region of absolute instability vanishes. The pattern of attenuating growth rate and shrinking region of absolute instability can be easily verified by comparing table 3, showing the evolution of the maximum temporal growth rate,  $\omega_i$ , and absolute growth rate,  $\omega_{0i}$ , with varying  $x_0$ , when  $Fr = 15$ , with table 1. In analogy with figure 9(a,b), figure 11(a,b) shows the evolution of growth rate  $\alpha_i$  with varying wavenumber  $\alpha_r$  for different values of  $Fr$  at the streamwise locations  $x_0 = 0.6$  and  $2.5$ ;  $\omega_i = 0$ . Unlike  $We$ ,  $Fr$  basically affects moderate wavenumbers. Given the tendency of  $\alpha_i$  versus  $\alpha_r$  curves

$x_0$	$\omega_{i,max}$	$\omega_{0,i}$
1.2	1.0	-0.017
1.5	1.2	0.049
2.0	1.5	0.096
2.5	1.66	0.088
3.0	1.78	0.047
3.5	1.89	-0.018
5.0	2.1	-0.302

TABLE 2. Evolution of the maximum growth rate,  $\omega_{i,max}$ , and the absolute growth rate,  $\omega_{0,i}$ , of interfacial waves with increasing streamwise location,  $x_0$ , on the plate for the air–water system;  $\rho/\rho_w \approx 0.001$ ,  $\mu/\mu_w \approx 0.018$ ,  $Fr \approx 30$ ,  $We^{-1} \approx 350$ .

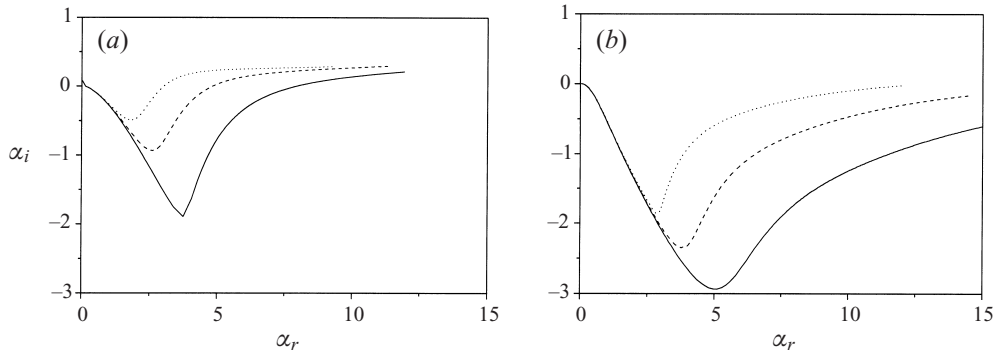


FIGURE 9. Evolution of the growth rate,  $\alpha_i$ , versus  $\alpha_r$  for the interfacial mode with varying  $We$ .  $\omega_i = 0$ ,  $Fr \approx 30$ ; —,  $We^{-1} = 66$ ; - - -,  $We^{-1} = 150$ ; ·····,  $We^{-1} = 350$ . (a)  $x_0 = 0.6$ , (b)  $x_0 = 3.4$ .

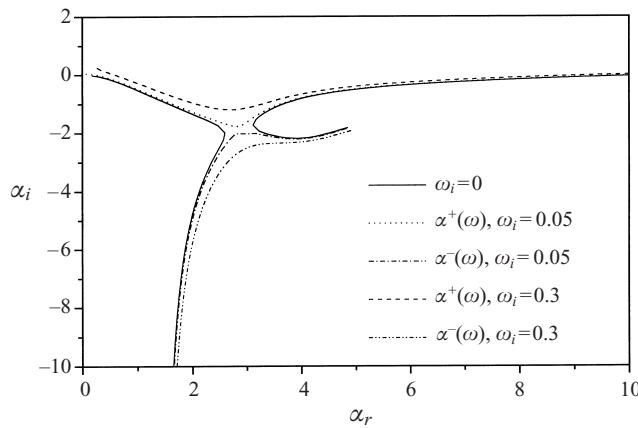


FIGURE 10. Pinching diagram for the interfacial mode;  $x_0 = 3$ ,  $Fr = 30$ ,  $We^{-1} = 350$ .

in this family to progressively include larger values of  $\alpha_r$  in the unstable regime as  $x_0$  increases, decreasing  $Fr$  results in attenuating the maximum growth rate of a wider range of wavenumbers thus making pinching harder. In fact, the family becomes absolutely unstable when  $Fr$  attains the value of 60 and 30 for the cases shown in figures 11(a) and 11(b) respectively. This can also be seen in figure 12, which shows

$x_0$	$\omega_{i,max}$	$\omega_{0,i}$
0.6	1.38	-0.109
0.7	1.57	-0.389
0.8	1.73	0.012
1.0	1.97	0.063
1.2	2.18	0.063
1.4	2.39	0.026
1.5	2.4	-0.002
3.0	2.93	-0.896

TABLE 3. Evolution of the maximum growth rate,  $\omega_{i,max}$ , and the absolute growth rate,  $\omega_{0,i}$ , of interfacial waves with increasing streamwise location,  $x_0$ , on the plate for the air-water system;  $\rho/\rho_w \approx 0.001$ ,  $\mu/\mu_w \approx 0.018$ ,  $Fr \approx 15$ ,  $We^{-1} \approx 66$ .

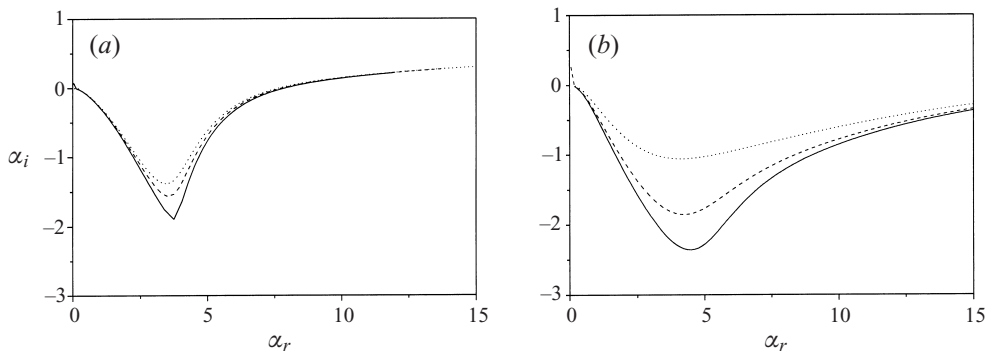


FIGURE 11. Evolution of the growth rate,  $\alpha_i$ , versus  $\alpha_r$  for the interfacial mode with varying  $Fr$ .  $\omega_i = 0$ ,  $We^{-1} \approx 66$ ; (a)  $x_0 = 0.6$ , —,  $Fr = 30$ ; - - -,  $Fr = 15$ ; ·····,  $Fr = 10$ , (b)  $x_0 = 2.5$ , —,  $Fr = 15$ ; - - -,  $Fr = 10$ ; ·····,  $Fr = 5$ .

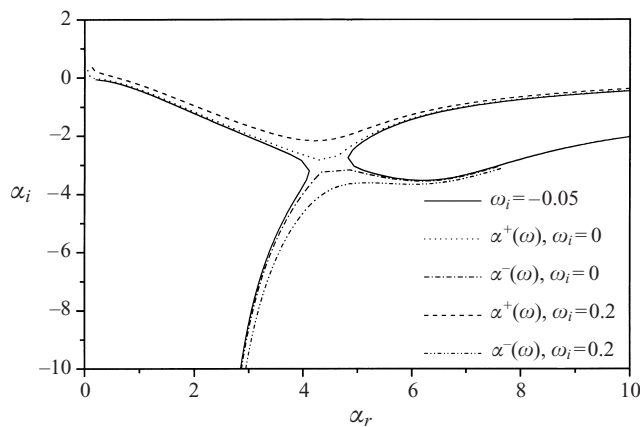


FIGURE 12. Pinching diagram for the interfacial mode;  $x_0 = 1.5$ ,  $Fr = 15$ ,  $We^{-1} = 66$ .

the pinching process for the case  $We^{-1} \approx 66$ ,  $Fr \approx 15$ ,  $x_0 = 1.5$ ; pinching occurs when  $\omega_i = -0.002$  and the family is convectively unstable. This situation is similar to the one shown in figure 6(a) with the exception that in the latter case  $Fr = 30$ , pinching occurs when  $\omega_i = 0.304$  and the family is absolutely unstable.

The effect of rainfall rate  $\dot{r}$  and free-stream velocity  $U_\infty$  on the stability characteristics of the system was also examined. If  $L = 30$  cm is the length of the plate and  $L^*$  is chosen so that  $H_f(L^*) \approx L^* Re^{5/8}(L^*)$ , with  $H_f$  given by (2.13), then increasing the rainfall rate amounts to decreasing  $L^*$  while increasing  $We^{-1}$  and  $Fr$  like  $\dot{r}^{5/6}$ . Keeping this in mind, the stability characteristics of the air–water system are examined when  $Fr \approx 146$ ,  $We^{-1} \approx 329$ . This amounts to increasing the rainfall rate by a factor of 5 ( $\dot{r} = 500$  mm h<sup>-1</sup>). The combined effect brought about by varying both  $We$  and  $Fr$  is that the pocket of absolute instability of interfacial waves now becomes  $1.2 \leq x_0 \leq 6$ . As expected from the findings of the parametric study presented above, the range of absolute instability is transferred to larger streamwise locations due to the higher  $We^{-1}$  value, whereas increasing  $Fr$  results in a significant widening of this range. However, the dimensional distance at which absolute instability arises is decreased, compared to the case with lower rainfall rate, owing to the decrease of the characteristic length  $L^*$  needed for the film thickness to reach the triple-deck size with increasing rainfall rate. In fact  $L^* \propto \dot{r}^{-4/3}$ . Consequently increasing the rainfall rate by a factor of 5 amounts to decreasing the value of  $L^*$  for which  $x_0 = 1$  by, roughly, 8.5 times. Since, on the other hand, the interval of absolute instability extends up to  $x_0 = 6$ , for given length of the test wing section,  $L$ , almost the entire section is immersed in a flow that is absolutely unstable. Finally the stability of the system was examined for a case with lower free-stream velocity,  $U_\infty = 20$  m s<sup>-1</sup>. The corresponding  $Fr$  and  $We^{-1}$  are 6.7 and 234.5, respectively. In this case both waves remain convectively unstable for the entire range of  $x_0$  values examined. In general, increasing the free-stream velocity tends to increase  $Fr$  while decreasing  $We^{-1}$ , thus widening the pocket of absolute instability and increasing the growth rate of unstable waves.

The findings of the present study demonstrate the importance of interfacial waves in boundary layer stability in the presence of a growing water film. Unlike temporal analysis, the approach adopted here allows a more general class of local flow perturbations that is closer to practices often used in experimental investigations and that is deemed to be pertinent to the problem of airfoil stability under conditions of rainfall. In this case the pocket of absolute instability which is found to arise, in the parameter range relevant to our problem, is conjectured to give rise to a global mode that interacts intensely with the boundary layer, thus deteriorating airfoil performance. Clearly further analysis is warranted in order to verify the global characteristics of the flow as well as the effect of nonlinearity on growing waves.

This research was supported by Greek Secretariat of Research & Technology under the PENED 95 grant 58 and the Greek Ministry of Education under the EPEAEK program. The first author also wishes to thank Professor Acrivos for providing him with the original NASA reports that instigated his interest in the subject.

#### REFERENCES

- BENJAMIN, T. B. 1958 Shearing flow over a wavy boundary. *J. Fluid Mech.* **6**, 161–205.
- BERS, A. 1975 Linear waves and instabilities. In *Physique des Plasmas* (ed. C. DeWitt & J. Peyraud), pp. 117–215. Gordon & Breach.
- BOELEN, O. J. & HOEIJMAKERS, H. W. M. 1997 Wave formation on de-/anti-icing fluids. *Paper presented at the 3rd European Mechanics Conference (EUROMECH), Goettingen, Germany* (unpublished).
- BRIGGS, R. J. 1964 *Electron-Stream Interaction with Plasmas*. MIT Press.
- CAMPBELL, B. A. & BEZOS, M. 1989 Steady-state and transitional aerodynamic characteristics of a wing in simulated heavy rain. *NASA TP-2932*.

- CARBONARO, M. & OZGEN, S. 1997 Aerodynamic effects of de-/anti-icing fluids and description of a facility and test techniques for their aerodynamic acceptance. *Lecture presented at the AGARD-FDP-VKI Lecture Series on the Effect of Icing, De-icing and Heavy Rain on Aircraft Performance*. Von Karman Institute for Fluid Dynamics, Belgium.
- DRAZIN, P. G. & REID, W. H. 1981 *Hydrodynamic Stability*. Cambridge University Press.
- DUNHAM, R. E. JR. 1987 The potential influence of rain on airfoil performance. *Lecture presented at the Von Karman Institute for Fluid Dynamics, Belgium*.
- FEO, A. & GONZALEZ, P. 1988 Water film thickness measurements on an airfoil surface in a water-spray from NASA-Langley's  $4 \times 7$  meter wind tunnel tests. *INTA N/221/510/89.004*.
- GASTER, M. 1962 A note on the relation between temporally-increasing and spatially-increasing disturbances in hydrodynamic stability. *J. Fluid Mech.* **14**, 222–224.
- GASTER, M. 1965 On the generation of spatially growing waves in a boundary layer. *J. Fluid Mech.* **22**, 433–441.
- HAPPEL, J. & BRENNER, H. 1986 *Low Reynolds Number Hydrodynamics*. Martinus Nijhoff.
- HEALEY, J. J. 1995 On the neutral curve of the flat plate boundary layer: comparison between experiment, Orr-Sommerfeld theory and asymptotic theory. *J. Fluid Mech.* **288**, 59–73.
- HENGST, J. VAN 1991 Flight test of the aerodynamic effect of type I and type II ground de-/anti-icing fluids on the fokker 50 and fokker 100 aircraft. *AIAA Paper* 91–0785.
- HOOPER, A. P. 1985 Long-wave instability at the interface between two viscous fluids: thin layer effects. *Phys. Fluids* **28**, 1613–1618.
- HOOPER, A. P. & BOYD, W. G. C. 1987 Shear-flow instability due to a wall and a viscosity discontinuity at the interface. *J. Fluid Mech.* **179**, 201–225.
- HUERRE, P. & MONKEWITZ, P. A. 1985 Absolute and convective instabilities in free shear layers. *J. Fluid Mech.* **159**, 151–168.
- HUERRE, P. & MONKEWITZ, P. A. 1990 Local and Global Instabilities in Spatially Developing Flows. *Ann. Rev. Fluid Mech.* **22**, 473–537.
- HULTGREN, L. S. 1987 Higher eigenmodes in the Blasius boundary-layer stability problem. *Phys. Fluids* **30**, 2947–2951.
- JORDINSON, R. 1970 The flat plate boundary layer. Part 1. Numerical integration of the Orr-Sommerfeld equation. *J. Fluid Mech.* **43**, 801–811.
- LINGWOOD, R. J. 1995 Absolute instability of the boundary layer on a rotating disk. *J. Fluid Mech.* **299**, 17–33.
- LINGWOOD, R. J. 1997 On the application of the Briggs and steepest-descent methods to a boundary-layer flow. *Stud. Appl. Maths* **98**, 213–254.
- MESSITER, A. E. 1970 Boundary-layer flow near the trailing edge of a flat plate. *SIAM J. Appl. Maths* **18**, 241–257.
- NEILAND, V. YA. 1969 Towards a theory of separation of the laminar boundary layer in a supersonic stream. *Izv. Akad. Nauk SSSR, Mekh. Zhidk. Gaza* **4**, 33–35.
- NELSON, J. J., ALVING, A. E. & JOSEPH, D. D. 1995 Boundary layer flow of air over water on a flat plate. *J. Fluid Mech.* **284**, 159–169.
- OZGEN, S., DEGREZ, G. & SARMA, G. S. R. 1998 Two-fluid boundary layer stability. *Phys. Fluids* **10**, 2746–2757.
- PELEKASIS, N. A. & ACRIVOS, A. 1995 Forced convection and sedimentation past a flat plate. *J. Fluid Mech.* **294**, 301–321.
- PELEKASIS, N. A., TSAMOPOULOS, J. A. & MANOLIS, G. D. 1992 A hybrid finite-boundary element method for inviscid flows with free surface. *J. Comput. Phys.* **254**, 501–527.
- SMITH, F. T. 1979 On the non-parallel flow stability of the Blasius boundary layer. *Proc. R. Soc. Lond. A* **366**, 91–109.
- SMITH, F. T., BRIGHTON, P. W. M., JACKSON, P. S. & HUNT, J. C. R. 1981 On boundary-layer flow past two-dimensional obstacles. *J. Fluid Mech.* **113**, 123–152.
- SMYRNAIOS, D. N., PELEKASIS, N. A. & TSAMOPOULOS, J. A. 2000 Boundary layer flow of air past solid surfaces in the presence of rainfall. *J. Fluid Mech.* **425**, 79–110.
- STEWARTSON, K. & WILLIAMS, P. G. 1969 Self induced separation. *Proc. R. Soc. Lond. A* **312**, 181–206.
- THOMSON, B. E., JANG, J. & DION, J. L. 1995 Wing performance in moderate rain. *J. Aircraft* **24**, 1034–1039.
- TIMOSHIN, S. N. 1997 Instabilities in a high-Reynolds-number boundary layer on a film-coated surface. *J. Fluid Mech.* **353**, 163–195.

- TSAO, J. C., ROTHMAYER, A. P. & RUBAN, A. I. 1997 Stability of air flow past thin liquid films on airfoils. *Computers Fluids* **26**, 427–452.
- YIANTSIOS, S. G. & HIGGINS, B. G. 1998 Linear stability of plane Poiseuille flow of two superposed fluids. *Phys. Fluids* **31**, 3225–3238.
- YIH, C.-S. 1967 Instability due to viscosity stratification. *J. Fluid Mech.* **212**, 41–53.